ACS APPLIED POLYMER MATERIALS

pubs.acs.org/acsapm Article

Beyond Conventional: Antibacterial, Antioxidant, and Photocatalytic Properties of Nanofibers Featuring Metal-Oxide-Modified Boron Nitride Nanoparticles

Nesrin Horzum, Deniz Doğan, Fatma Rabia Karaduman, and Ayşegül Ülkü Metin*

Cite This: *ACS Appl. Polym. Mater.* 2024, 6, 3942−3955 Read Online

ACCESS | Metrics & More | Article Recommendations | Supporting Information

ABSTRACT: CuO-, ZrO_2-, and ZnO-immobilized functional boron nitride (fBN) nanoparticles were synthesized by an environmentally friendly approach using a *Stevia rebaudiana* extract. Metal-oxide-immobilized fBN nanoparticles (fBN/MO)-incorporated (1 wt %) polyvinyl alcohol/poly(acrylic acid) composite nanofibers were fabricated by electrospinning, and their antibacterial, antioxidant, and photocatalytic properties were investigated. fBN/CuO and fBN/ZnO nanoparticles were distributed randomly, showcasing nonuniform geometries besides polygonal-shaped fBN/ZrO_2 nanoparticles. fBN/MO nanoparticles exhibited a uniform dispersion along the composite nanofibers, with diameters between 115 and 160 nm. The incorporation of fBN/MO nanoparticles into the composite nanofibers (0.074−0.753 W/mK) resulted in an improvement in both thermal stability and conductivity when compared with PVA/PAA nanofibers (0.063 W/mK). fBN/MO-modified composite nanofibers exhibited an antibacterial efficacy exceeding 99% against *Streptococcus mutans*, *Acinetobacter baumannii*, *Escherichia coli*, and *Staphylococcus aureus*, augmenting their antioxidant properties. The modified composite nanofibers, particularly those incorporating fBN/ZrO_2 nanoparticles, exhibited effective photocatalytic remediation against methylene blue (MB) with the highest activity, attributed to their favorable morphological and optoelectronic properties, resulting in a remarkably more than 20-fold improvement. Enhanced stability for repeated treatment of MB for a minimum of three cycles was achieved. The multifunctional nature of nanofibers unveils synergistic antibacterial, antioxidant, and photodegradation effects, positioning them as promising for biomaterials and water disinfection.

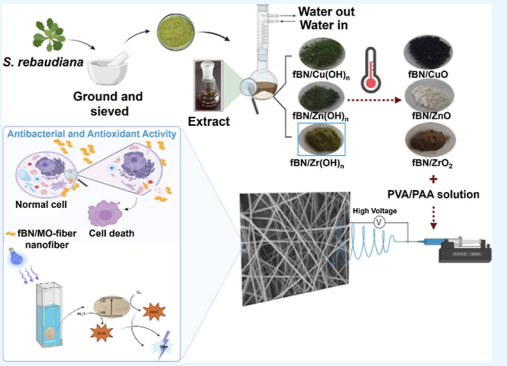

KEYWORDS: *boron nitride, electrospinning, nanofibers, poly(vinyl alcohol), poly(acrylic acid), thermal conductivity*

INTRODUCTION

Water pollution is one of the most important environmental problems today because of increasing industrialization. The main pollutants are nutrients, halogens, heavy metals, pesticides, dyes, microplastics, oil, suspended solids and sediment, thermal enrichment, and radioactive wastes.[1] Dye pollution in water resources significantly threatens human health, aquatic organisms, and entire ecosystems. Over 700,000 tons of 100,000 commercial paints are produced annually for use in various industries,[2] and approximately 10−15% of dyes are discharged into water streams.[3] Dyes are widely used in various industries, such as textiles, paper, leather tanning, plastics, rubber, paint manufacturing, cosmetics, food, agriculture, pharmaceuticals, and electroplating.[4] Even at very low concentrations, dyes alter the transparency and esthetics of water and hence affect photosynthetic activity, reduce gas solubility in water, and inhibit the growth of aquatic organisms.[2] It also causes serious damage to human health, such as mutagenic effects, respiratory problems, kidney and liver dysfunction, reproductive system and central nervous system disorders, cancer, behavioral problems, and allergic reactions, depending on concentrations and exposure times.[5] For this reason, researchers focus on specific methods and technologies such as adsorption, coagulation, flocculation, advanced oxidation process, membrane separation, oxidation, ion exchange, electrochemical process, photocatalysis, and biodegradation for the remediation of dyes from wastewater.[6] Dye removal processes are expected to be able to effectively remove large quantities of dyes in a short period of time without generating secondary waste.[7] Among the aforementioned methods, photocatalytic degradation is an efficient, environmentally friendly, low-cost, and sustainable heterogeneous advanced oxidation process.[8] In addition, this method has significant advantages such as complete degradation and

Received: December 30, 2023
Revised: February 14, 2024
Accepted: March 15, 2024
Published: March 28, 2024

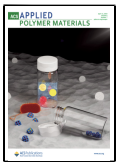

https://doi.org/10.1021/acsapm.3c03226
ACS Appl. Polym. Mater. 2024, 6, 3942−3955

mineralization of even very stable dyes to CO_2, H_2O, and mineral acids.

An ideal photocatalyst should have high adsorption capacity and surface area, efficient charge separation, high mobility of charge carriers, and light absorption.[9] Various materials, such as metal oxides (MOs), metal sulfides, magnetic compounds, doped semiconductors, metal−organic frameworks, hybrid compounds, and carbon-based nanomaterials, have been used as photocatalysts for the degradation of dyes. Among them, MOs have well-controlled surface structure properties and can be used as semiconductors with wide band gaps. In addition, their nontoxicity and stability make them prominent in the photocatalytic degradation of dyes.[10] MOs such as ZnO, TiO_2, CeO_2, CuO, SnO_2, Bi_2O_3, WO_3, Al_2O_3, NiO, ZrO_2, Fe_3O_4, and MnO_2 are widely used as photocatalysts.[10,11] In a study on TiO_2, Verma et al.[12] investigated the degradation of malachite green and methylene blue (MB) using TiO_2 nanoparticles with graphene oxide nanocomposites via the sol−gel method. Jemai et al. tested the photocatalytic degradation of amido black dye with amorphous and annealed ZrO_2 nanotubes synthesized using the electrochemical anodization method.[13]

Recently, biogenic synthesis of metal or MO nanoparticles is also preferred because plant extracts, algae, bacteria, fungi, yeast, etc., act as natural reducing and/or stabilizing agents. Chelliah et al. synthesized ZrO_2 nanoparticles using the *Murraya koenigii* leaf extract and investigated the photocatalytic degradation of MB under visible-light irradiation.[14] *Thymus vulgaris* leaf and citrus lemon seed extracts were employed to obtain ZnO nanoparticles that are used for the degradation of MB and Sunfix Red[15] and Remazole Brilliant Blue R,[16] respectively. Similarly, the photocatalytic activities of *Seriphidium oliverianum*,[17] *Ocimum tenuiflorum*,[18] and papaya/lemon tea[19] extracts-based CuO nanoparticles were investigated against methyl orange. For this purpose, an extract obtained from *Stevia rebaudiana*, a plant species belonging to the Stevia genus within the Asteraceae family,[20] was employed for the synthesis of MO nanoparticles. The extract, enriched with bioactive compounds, serves as a biogenic precursor for controlled and sustainable MO synthesis. This bioinspired approach not only harnesses the inherent properties of *S. rebaudiana* but also aligns with the principles of green chemistry.

Nowadays, organic and inorganic additives such as transition metals (Fe, Cu, Ni, Ce, Ag), nonmetal elements (B, C, N, S, P), oxide (TiO_2, CuO, ZnO, Bi_2O_3, WO_3, CdO) and nonoxide (BN, TiN, MoN, WC, SiC) ceramics, metal halides (PbX_2, AgX, CuX), conductive polymers (PANI, PPy, PTh), etc. were employed to improve the photocatalytic activity of MOs.[21,22] Among them, boron nitride (BN) has attracted considerable attention with a two-dimensional hexagonal network with structural similarity to graphene.[23] It exhibits a high surface area, chemical stability, mechanical strength, thermal conductivity, and optical and catalytic properties. BN is also a typical insulator with a large band gap of 5−6 eV in its pure state.[24] Therefore, adding BN is used to adjust the band gap of the MO, increasing the charge separation capability and providing a way to improve the separation efficiency of photogenerated electron−hole pairs.[25] Many researchers have reported studies combining BN with MOs such as BN/SnO_2,[26] BN/WO_3,[27] BN/TiO_2,[25] and BN/ZnO.[28] Liu et al. synthesized a heterostructure photocatalyst based on ZnO nanoparticles decorated with BN QDs and reported that it exhibited exceptional photocatalytic performances and high stability for the degradation of MB and methyl orange under UV-light irradiation.[28] Xu et al. investigated the photocatalytic activity of the BN/WO_3 hybrid material for rhodamine B, and even a small amount of BN was reported to be sufficient for enhanced photocatalytic activity compared to neat WO_3.[27] According to Singh et al., the accumulation of SnO_2 on BN nanosheets provides a high surface area, transforming the particles into a suitable form for catalytic processing.[26]

One of the nanostructures with a high surface area is electrospun nanofibers, which provide an advantage compared to powder materials by serving as a structural framework.[29] Electrospinning is a relatively robust, simple, and effective technique for producing nanofibers from various polymers.[30] The high surface area/volume ratio, tunable porous structure, and flexibility of the nanofibers provide a large contact surface between the photocatalyst and pollutants, thus increasing the photocatalytic activity.[31] In a study by Nasr et al., high-activity BN/TiO_2 composite nanofibers were used as a photocatalyst for the degradation of methyl orange under UV-light irradiation.[25] Abid et al. produced nontoxic composite fibers containing varying amounts of BN nanosheets (0, 3, 5, and 10 wt %), TiO_2 nanofibers, and halloysite nanotubes and used them for acetaminophen (ACT) degradation.[32] Ghorbanloo et al. synthesized BN/Cs_2CO_3/TiO_2 nanofibers for hydrogen production.[33] Lin et al. fabricated TiO_2-BN-enabled electrospun nanofibers for visible-light photocatalytic treatment of ibuprofen and secondary wastewater effluents.[34] Sayegh et al. tested the photocatalytic degradation of ACT by producing electrospun TiO_2/BN/Pd nanofibers.[35] In another study, a boron-doped graphitic carbon nitride (B-C_3N_4) photocatalyst was synthesized and blended with polyethersulfone and poly(vinylpyrrolidone) to fabricate composite nanofibrous membranes and were used in the degradation of methyl orange.[36] On the other hand, reported studies on the fabrication and usage of BN/MO-modified electrospun nanofibers as photocatalysts for dye degradation are still limited.

In this study, MO nanoparticles (CuO, ZnO, and ZrO_2) were decorated onto the fBN nanoparticles using the extract of *S. rebaudiana* plant leaves to enhance the antibacterial efficacy, antioxidant characteristics, and photocatalytic efficiency. To establish a structural framework and improve the mechanical integrity of fBN/MO nanoparticles, they were converted into electrospun nanofibers using the PVA/PAA composite system. To the best of our knowledge, no research has been conducted on the fabrication of BN/MO-modified electrospun nanofibers and evaluation of their structural and morphological properties as well as biological and photocatalytic activities.

EXPERIMENTAL SECTION

Materials and Chemicals. Boron nitride (BN; 50 nm 99.9%) was obtained from Nanotech. (3-Aminopropyl)trimethoxy silane (APTMS), polyvinyl alcohol (PVA, Mn ∼ 30.000−70.000 g mol^{-1}, 87−90% hydrolyzed), and poly(acrylic acid) (PAA, M_w ∼ 450.000 g mol^{-1}) were obtained from Sigma-Aldrich. Zinc chloride ($ZnCl_2$, 99.9%) was obtained from Merck, copper(II) sulfate pentahydrate ($CuSO_4{\cdot}5H_2O$, 97.07%) was obtained from Kimetsan, and zirconium oxychloride ($ZrOCl_2$, 97%) was obtained from Fluka. All other chemicals were of analytical grade and purchased from Merck.

Synthesis of fBN/MO Nanoparticles. BN (1.0 g, mean size ≤ 50 nm) was first treated with 40 mL of ethanol in an ultrasonic bath (600 W) for 30 min. Then, APTMS, glutaraldehyde (GA), and L-histidine (L-his) were used for BN layer activation. For this purpose, 1 mL of APTMS was added to BN (1.0 g), dispersed in ethanol (40 mL), and

https://doi.org/10.1021/acsapm.3c03226
ACS Appl. Polym. Mater. 2024, 6, 3942−3955

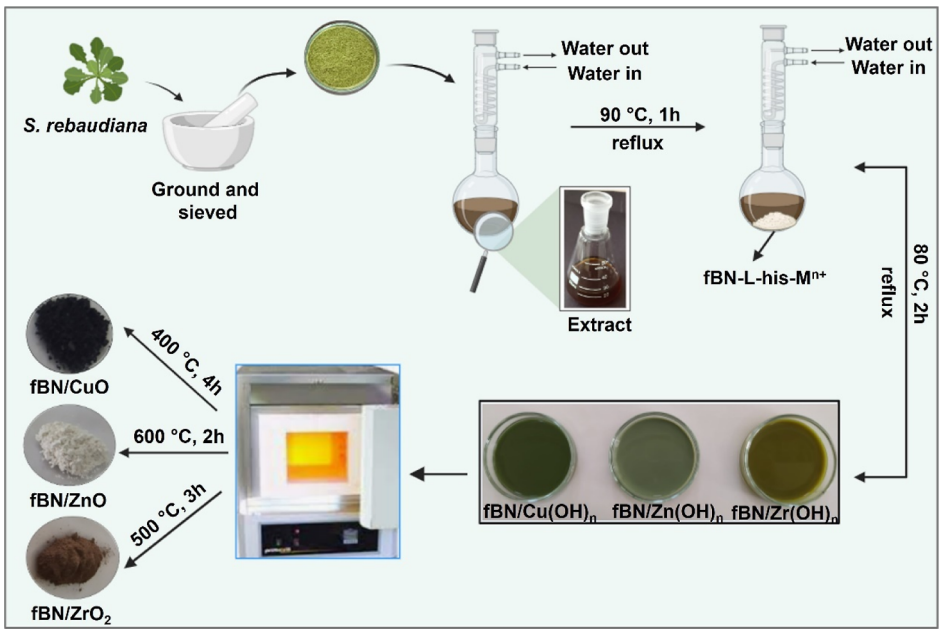

Figure 1. Pictorial representation of the synthesis of fBN/MO nanoparticles.

shaken in a water bath at 60 °C for 16 h. After the reaction, APTMS-modified BN was separated from the solution by centrifugation and washed three times with distilled water.[37] The modified BN was first equilibrated in 40 mL of phosphate-buffered saline (PBS, pH 7.4) for 6 h and then incubated in GA solution (0.5%) for a further 12 h. Excess GA was removed by washing the nanoparticles with distilled water, acetic acid solution, and PBS. The GA-activated nanoparticle was incubated with L-his solution (2 mg/mL, 25 mL) for 24 h,[38] and the obtained nanoparticles, abbreviated as fBN-L-his, were washed with distilled water and PBS.

fBN-L-his nanoparticles (1.0 g) were incubated with metal salts (40 mL) in the concentration range of 10−200 mM at room temperature for 6 h and then centrifuged. Metal-ion-immobilized fBN-L-his nanoparticles (fBN-L-his-M^{n+}) were washed three times with distilled water. fBN-L-his-M^{n+} layers were converted to metal hydroxyls by phytosynthesis. For this purpose, an extract of *S. rebaudiana* leaves was obtained as follows: *S. rebaudiana* leaves were ground in an herbal grinder and sieved (<45 μm). It (2.0 g) was treated in 40 mL distilled water at 90 °C for 1 h under reflux, then cooled to room temperature, and the filtrate was separated by centrifugation.[39] The fBN-L-his-M^{n+} nanoparticles were added to the extract (40 mL) and stirred under reflux for 2 h at 80 °C, followed by centrifugation. The obtained products were dried in an oven at 100 °C for 1 h and were abbreviated as fBN/Cu(OH)n, fBN/Zr(OH)n, and fBN/Zn(OH)n. Metal hydroxides (fBN/(MO)n) were converted into MO by applying heat treatment ranging from 400 to 600 °C for 2−4 h (Figure 1).

Fabrication of fBN/MO-Modified Composite Nanofibers. An aqueous polymer solution was prepared from PVA (20 wt %) and PAA (1 wt %), and then fBN/CuO, fBN/ZrO_2, and fBN/ZnO nanoparticles were dispersed in the PVA/PAA solution at concentrations of 1 wt % and homogenized by an ultrasonicator (180 W, 15 min). PVA/PAA composite nanofibers containing fBN/MO nanoparticles were fabricated by electrospinning. An Inovenso basic setup was used by adjusting the flow rate to 1 mL/h with the help of a microinfusion pump. A voltage of about 14 kV and a 17 cm needle-to-collector distance were applied. Each polymeric solution was electrospun for 4 h to control the thickness of the mats. Then, the obtained mats were heat-treated at 135 °C for 80 min.[40]

Morphological and Structural Characterizations of fBN/MO Nanoparticles and fBN/MO-Modified Composite Nanofibers. The formation of metal nanoparticles from the *S. rebaudiana* extract was controlled by a UV−vis spectrometer (Shimadzu, model 1280, Tokyo, Japan). The crystallinity of BN and fBN/MO nanoparticles was obtained using an X-ray diffractometer (Bruker AXS/Discovery D8) in the range of 10−90° at a scanning speed of 1°/min. Morphological properties of BN and fBN/MO nanoparticles were investigated using a scanning electron microscope (GAIA3, TESCAN, Germany), and the elemental compositions were also determined using an SEM/EDX system (Carl Zeiss 300VP, Germany). The hydrodynamic diameters of fBN/MO nanoparticles were determined using a Zetasizer (Nano-2S-ZEN 3600, Malvern Instruments, UK).

BN and fBN/MO nanoparticles, PVA/PAA, and fBN/MO-modified composite nanofibers were analyzed by using an FTIR spectrometer (Bruker Vertex 70V). The surface properties of PVA/PAA and fBN/MO-modified composite nanofibers and their elemental compositions were determined using an SEM/EDX system (Carl Zeiss 300VP, Germany). The average fiber diameters of the nanofibers were calculated from SEM images by using at least 100 randomly selected fibers with the Fiji program.

The thermal properties of PVA/PAA and fBN/MO-modified composite nanofibers were determined using a TGA/DSC instrument (TA/SDT650).[41,42] The thermodynamic functions were calculated using the Coast−Redfern equation given in eq 1

$$\log\left[\log\frac{\log Ws/(Ws-W)}{T^2}\right] = \log\left[\frac{AR}{\theta Ea}\left(1-\frac{2RT}{Ea}\right)\right] - \frac{Ea}{2303RT} \quad (1)$$

where W and Ws are instantaneous and final mass (mg) of the samples, respectively. R is the gas constant (J/molK), and θ is the heating rate (K/min). The activation energy (Ea, J/mol) was determined from the slope of the line obtained from the $\log\left[\log\frac{\log Ws/(Ws-W)}{T^2}\right]$ versus $1/T$ plot.[42] Changes in enthalpy (ΔH), entropy (ΔS), and Gibbs free energy (ΔG) were calculated with eq 2.

$$\Delta H = Ea - RT; \qquad \Delta S = 2303R\left(\frac{Ah}{K_b T}\right);$$
$$\Delta G = \Delta H - T\Delta S \quad (2)$$

where h is the Planck constant and K_b is the Boltzmann constant.

The thermal conductivity (TC) of PVA/PAA and fBN/MO-modified composite nanofibers was determined by using a laser flash TC analyzer (Linseis LFA 1000, Germany). The composite

https://doi.org/10.1021/acsapm.3c03226
ACS Appl. Polym. Mater. 2024, 6, 3942−3955

nanofibers were prepared as pellets (10 × 0.2 mm) by pressing at 10 kN, and their surfaces were coated with graphite to prevent light scattering. At least 10 measurements were taken from each sample to determine the thermal diffusivity.

TC of the samples was calculated using eq 3

$$\lambda = \alpha \times \rho \times \varsigma \tag{3}$$

where λ (W/mK) is TC; α (cm^2/s) is the thermal diffusivity, and ρ (g/cm^3) and ς (j/g °C) are the density and heat capacity of the samples, respectively. Differential scanning calorimetry (DSC; HITACHI DSC 7020) was used to determine the heat capacity of the samples.

Biological Characterization of fBN/MO-Modified Composite Nanofibers. The antibacterial activity of fBN/MO-modified composite nanofibers was determined using *Streptococcus mutans, Acinetobacter baumannii, Staphylococcus aureus*, and *Escherichia coli* bacteria according to the previously published protocol.[40]

The antioxidant activity of PVA/PAA and fBN/MO-modified composite nanofibers was determined using 2,2-azino-bis-3-ethylbenzothiazoline-*p*-sulfonic acid (ABTS). Potassium persulfate ($K_2S_2O_8$, 2.45 mM) was added to the ABTS (7 mM, 3 mL) solution, stirred for 2 h, and then left in the dark for 12−16 h at room temperature for the generation of $ABTS^{+\bullet}$ radicals. 10 mg composite nanofibers were treated with the prepared solution, and the absorbance of the supernatant was measured at 748 nm at the sixth minute. The antioxidant activity and L-ascorbic acid equivalent activity (AEAC) of the composite nanofibers were calculated according to eqs 4 and 5, respectively[43]

$$\text{radical scavenging activity (RSA, \%)} = {A_{ABTS} - A_{Sample}}/{A_{ABTS}} \times 100 \tag{4}$$

$$\text{AEAC} = {\varepsilon_{Antioxidant}}/{\varepsilon_{L-Ascorbic\ acid}} \tag{5}$$

Photocatalytic Degradation. Photocatalytic degradation experiments of PVA/PAA and fBN/MO-modified composite nanofibers were performed with MB (10 mL, 50 ppm). PVA/PAA and fBN/MO-modified composite nanofibers used as catalysts were incubated with MB solutions in the UV reactor (Luzchem/LZC-EDU, Canada) (UV-C tube lamp, 8 W, 360 nm). MB concentration was determined by the UV−vis spectrophotometer at 25 °C. Time-dependent photocatalytic degradation experiments were conducted at pH 7.0, 1.0 g/L, and ambient temperature. The reusability of the fBN/MO-modified composite nanofibers was also investigated for five successive cycles. After each cycle, the photocatalysts were washed with distilled water, followed by treatment with fresh MB solution.

The MB degradation rate was investigated using the pseudo-first-order kinetic model as described in eq 6.[44]

$$\ln C_o/C_t = kt \tag{6}$$

where k is the rate constant and C_o and C_t are MB concentrations at initial and specific times (t), respectively.

RESULTS AND DISCUSSION

Structural and Morphological Properties of fBN/MO Nanoparticles. To synthesize fBN/MO, the surface of BN nanoparticles was activated with functional groups to enhance the immobilization affinity of metal ions with APTMS, GA, and L-his (Figure 2a). The deposition of metal ions on fBN-L-his nanoparticles increased by the specific coordination bonds between L-his and metal ions [Cu(II), Zn(II), and Zr(IV)] (Figure 2b). Multidentate ligands and metal ions formed complexes (metal chelates) based on the coordination between electron-donating groups and the cations.[45] Ligands with N, S, O, and P atoms are widely encountered in coordination complexes.[46] These ligands act as Lewis bases, providing pairs of electrons to form coordinate bonds with metal ions, which

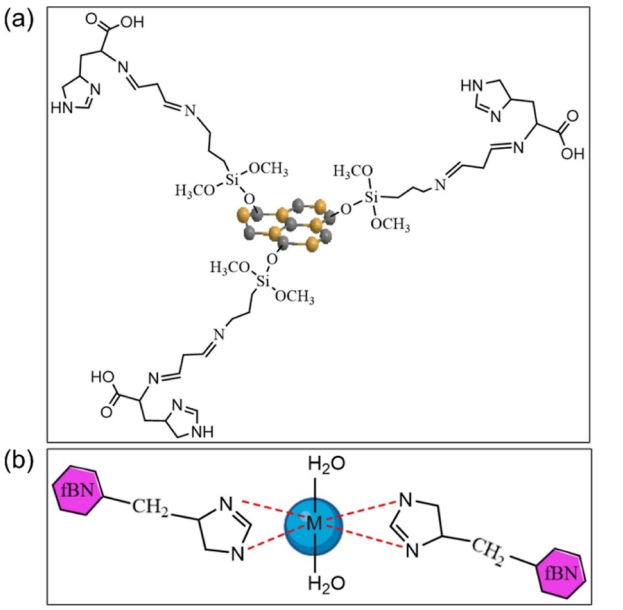

Figure 2. Schematic representation of the modification of BN (a) and the possible interaction of fBN-L-his and metal ions (b).

act as Lewis acids. The resulting coordination complexes often have distinctive structures and properties based on the nature of the ligands and the central metal ion. According to the hard and soft acid−base principle, boundary metal ions such as Co(II), Zn(II), Cu(II), and Ni(II), which are known to have medium hardness,[47] prefer to bind to soft Lewis acids such as N, S, O, and P atoms.[48]

The metal ions on fBN-L-his-M^{n+} nanoparticles were reduced by the *S. rebaudiana* extract. For comparison, the formation of metals and MO nanoparticles from the *S. rebaudiana* extract was also screened in the absence of fBN-L-his nanoparticles (Figure S1). Figure 3a shows the UV−vis spectra of fBN/MO nanoparticles. The extract obtained from the leaves of *S. rebaudiana* has absorbances at 329 and 290 nm and a strong absorbance at 207 nm. In addition, ketones and aromatic hydrocarbons in plant extracts and some chromophore groups, such as nitrite or α,β-enone, are also known to absorb light at a wavelength of 329 nm. Therefore, the peak around 329 nm originates from ketone groups of the extract.[49] fBN/CuO nanoparticles have maxima around 280 and 300 nm; for fBN/ZrO_2, it was observed at 273 nm, and for fBN/ZnO it was observed at 370 nm. The results are in good agreement with the literature.[50−52]

The crystal structure of BN and fBN/MO nanoparticles was evaluated by using XRD (Figure 3b). BN has characteristic signals at 26.88° (002), 41.96° (100), 55.46° (004), 76.08° (110), and 82.43° (110).[53,54] fBN/CuO has specific signals for Cu nanoparticles with a face-centered cubic structure observed at 75.16° (220), and for a monoclinic structure of CuO nanoparticles the signals were seen at 35.48° (002), 38.82° (111), 49° (200), 53.62° (020), 61.64° (113), 66.24° (311), and 68.14° (220).[55,56] For fBN/ZnO nanoparticles, the signals at 31.98° (100), 34.42° (002), 36.44°(101), 47.57° (102), 56.60° (110), 63.10° (103), 66.76° (200), 68.02° (112), 69.30° (201), and 72.76° (004) indicate the hexagonal-phased ZnO nanoparticles.[57] fBN/CuO and fBN/ZnO nanoparticles have a crystallinity index and a crystallite size of 62.51%, 107 nm and 73.76%, 208 nm, respectively. It is worth noting that factors like the calcination process, i.e., heating and cooling

https://doi.org/10.1021/acsapm.3c03226
ACS Appl. Polym. Mater. 2024, 6, 3942−3955

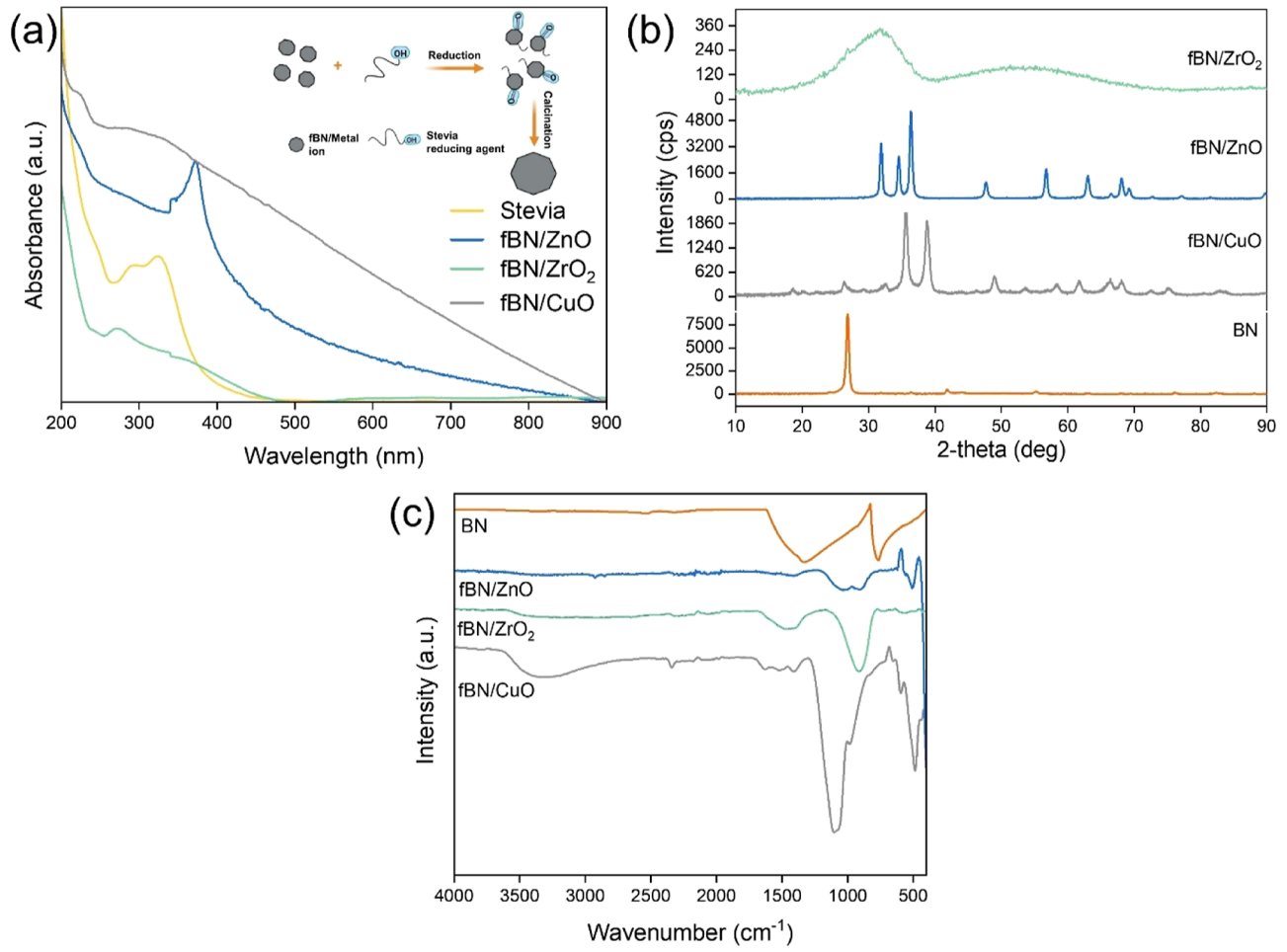

Figure 3. UV−vis spectrum of the *S. rebaudiana* extract and fBN/MO nanoparticles (a); XRD pattern (b) and FTIR spectra (c) of BN and fBN/MO nanoparticles.

rates and duration, can affect both the crystallinity and crystallite size.[58] The larger crystallites and higher crystallinity of fBN/ZnO nanoparticles can be attributed to the higher calcination temperature applied in the synthesis of fBN/ZnO nanoparticles. Diversely, the prepared fBN/ZrO_2 nanoparticles exhibit a structural disorder with broad signals corresponding to tetragonal (31.68°) and monoclinic (52.54°) phase reflections, in line with XRD patterns of amorphous ZrO_2.[59,60] In addition, the SEM micrograph of fBN/ZrO_2 supports this different behavior in the diffraction pattern.

The FTIR spectra of BN and fBN/MO nanoparticles are given in Figure 3c. At 1316 and 766 cm^{-1}, characteristic bands corresponding to in-plane B−N and B−N−B stretching vibrations are observed.[61] The band of Zn−O is seen at 516 cm^{-1},[52,54] while the peak of Zr−O is seen at 570 cm^{-1}.[62] The presence of the band of the Cu−O bond at 599 cm^{-1} indicates the MO conversion.[63] The bands of the −C−O vibrational band at 1091 cm^{-1} and the −OH vibrational band at 3336 cm^{-1} due to the steviol glycoside bond[64] are observed (Figure S2). For all spectra, the broad band belonging to the −OH group observed at approximately ∼3300 cm^{-1}, originates from the phenolic compounds surrounding the metal nanoparticles. In addition, the aromatic rings at 1512, 1620, and 1419 cm^{-1} are, respectively, attributed to C═C, C═O, and N−H vibrations of olefins, secondary amides, aldehydes, and ketones[49,64] originating from *S. rebaudiana,* APTMS, GA, and L-his (Figure S3). After the heat treatment, the intensity generally decreases; particularly, the higher intensity of fBN/CuO results from the lower calcination temperature applied.

Figure 4 demonstrates the morphological properties of BN and fBN/MO nanoparticles. The BN nanoparticles have a

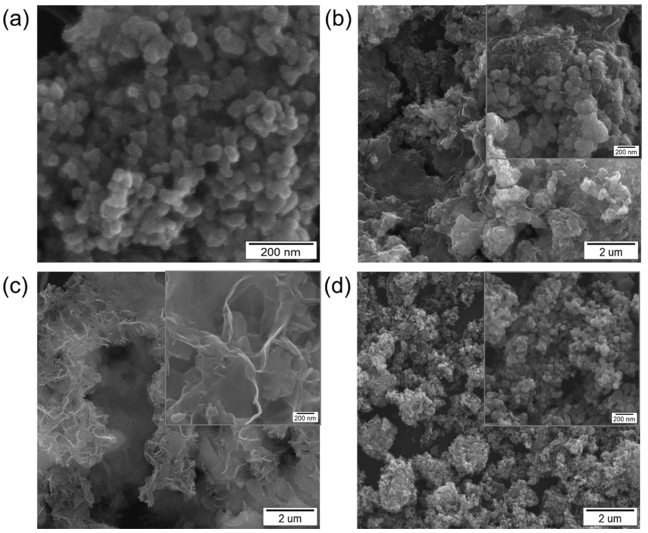

Figure 4. SEM micrographs of BN (a), fBN/CuO (b), fBN/ZrO_2 (c), and fBN/ZnO (d) nanoparticles.

https://doi.org/10.1021/acsapm.3c03226
ACS Appl. Polym. Mater. 2024, 6, 3942−3955

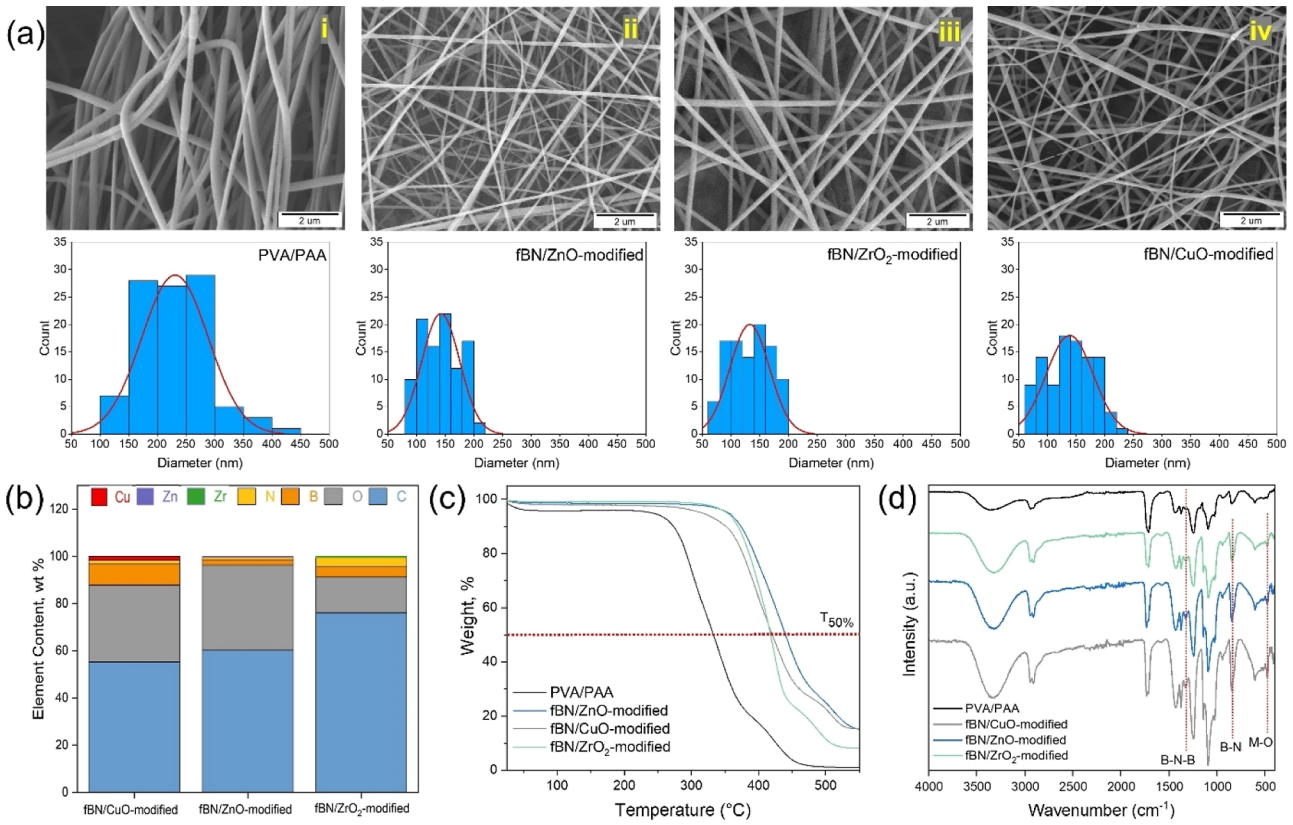

Figure 5. SEM micrographs and fiber diameter distribution (i—PVA/PAA, ii—fBN/ZnO, iii—fBN/ZrO_2, and iv—fBN/CuO-modified) (a), percent composition of elements (b), TGA curves (c), and FTIR spectra (d) of fBN/MO-modified nanofibers.

Table 1. Thermal Characteristics of Composite Nanofibers and Change in Thermodynamic Functions during Thermal Degradation of PVA/PAA and fBN/MO-Modified Composite Nanofibers (200 and 400 °C)

sample	TC (W/mK)	$T_{10\%}$ (°C)	$T_{50\%}$(°C)	Ea (kJ/mol)	ΔH (kJ/mol)	ΔG (kJ/mol)	ΔS (kJ/mol K)
PVA/PAA	0.063	273.31	332.81	16.85	12.50; 11.25	157.85; 199.98	−0.277; −0.279
fBN/ZnO-modified	0.227	373.63	440.03	18.01	14.07; 11.99	153.34; 227.37	−0.294; −0.297
fBN/CuO-modified	0.752	351.29	420.39	17.05	13.11; 11.04	151.22; 226.85	−0.292; −0.295
fBN/ZrO_2-modified	0.074	369.18	417.89	19.15	15.22; 13.14	151.23; 223.58	−0.287; −0.291

spherical geometry and a narrow size distribution. Though fBN/CuO and fBN/ZnO nanoparticles exhibit a random distribution with irregular geometry, fBN/ZrO_2 nanoparticles appear to adopt a polygonal geometry rather than a granular structure. The dissimilarities in morphological perspectives may arise from distinct interactions between the Zr(IV) ion and the phytochemicals found in the plant extract. Consistent viewpoints align with findings from prior studies in the literature, which highlighted the significant efficacy of plant extracts on the structural characteristics of resultant nanoparticles.[65] Previous research has underscored that phytochemicals present in plant extracts function not only as stabilizers but also as coating agents,[66] playing a crucial role in determining the structural properties of metal oxides (e.g., size, charge, stability, functionality, etc.).

The particle sizes of BN, fBN/CuO, and fBN/ZnO estimated statistically from SEM micrographs are approximately 38 ± 0.91, 86 ± 2.21, and 61 ± 3.58 nm, respectively. The hydrodynamic diameters of fBN/CuO, fBN/ZnO, and fBN/ZrO_2 nanoparticles were determined as 326.0 nm (PDI: 0.293), 216.7 nm (PDI: 0.240), and 216.9 nm (PDI: 0.272), respectively. The surface charges of fBN/CuO, fBN/ZnO, and fBN/ZrO_2 nanoparticles were measured as −23.3, −37.7, and −27.3 mV, respectively.

Morphological, Structural, and Thermal Characterizations of Nanofibers. The SEM micrographs, elemental compositions from EDS, and size distributions of fBN/MO-modified composite nanofibers are shown in Figure 5. Accordingly, fBN/MO-modified composite nanofibers are smooth, uniformly distributed, and bead-free, indicating that the fBN/MO particles are homogeneously incorporated along the composite fibers.

The average nanofiber diameters are 231 ± 16, 139 ± 15, 133 ± 16, and 142 ± 15 nm for PVA/PAA, fBN/CuO, fBN/ZrO_2, and fBN/ZnO-modified composite nanofibers, respectively (Figure 5a and b). The incorporation of fBN/MO caused a decrease in the nanofiber diameter, and almost equal-sized fBN/MO composite nanofibers with narrower distributions were obtained. Approximately 40% reduction in fiber diameter was observed due to intermolecular interactions between the template polymer and fBN/MO. Figure 5b confirms the presence of fBN/MO in/on the nanofibers. The distribution of fBN/MO nanoparticles along the fibers was also detailed through an EDS mapping analysis (Figure S4).

https://doi.org/10.1021/acsapm.3c03226
ACS Appl. Polym. Mater. 2024, 6, 3942−3955

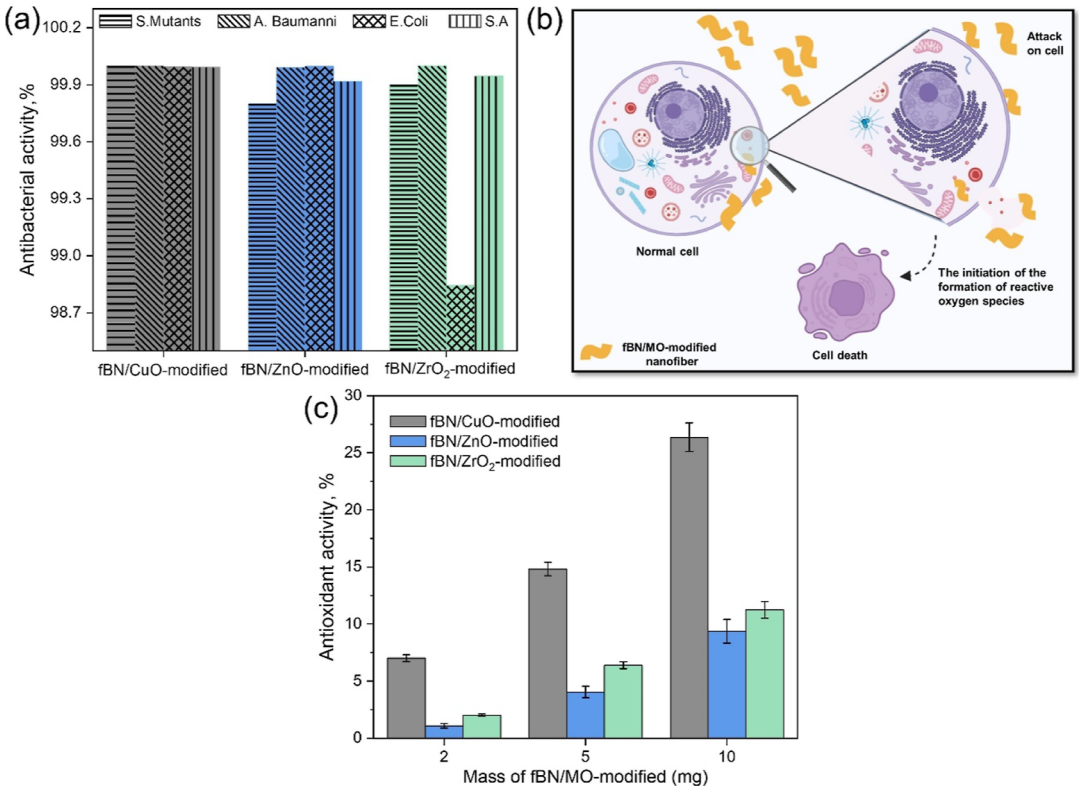

Figure 6. Antibacterial activity (a), schematic representation of the mechanisms leading to bacterial inhibition (b), and $ABTS^{+\bullet}$ scavenging activity (c) of fBN/MO-modified composite nanofibers.

The thermal degradation curves of PVA/PAA and fBN/MO-modified composite nanofibers (25−550 °C) are shown in Figure 5c. BN is thermally stable up to 800 °C without any weight loss.[67] The composite nanofibers have three thermal degradation steps, and the moisture and volatile/low-molecular-weight components are thought to be separated from the composite structures at temperature values where 10% weight loss occurs at the first stage. The thermal degradation step of 250−450 °C exhibited considerable weight loss due to the decomposition of the PVA/PAA chains. The temperature values at which 50% weight loss increased for fBN/MO-modified composite nanofibers compared to PVA/PAA nanofibers (Table 1) indicate enhanced thermal stability with the incorporation of fBN/MO because of the interfacial interaction between nanoparticles and the polymer matrix, improving the TC and reducing the rate of thermal degradation of composite fibers.[68] In addition to the inherent properties of the polymer and nanoparticles, other factors affecting the thermal performance of composite materials include nanoparticle agglomeration, particle size, functional groups on the particle surface, nanoparticle network in the polymer matrix, and surface energy of the polymer/nanoparticle system.[69] Among the MOs employed, fBN/ZnO increased the thermal stability the most.

The changes in thermodynamic functions were calculated using the Coats-Redfern method from the TGA curves of PVA/PAA and fBN/MO-modified composite nanofibers (Table 1). Accordingly, it was determined that the change in the Ea was determined as PVA/PAA < fBN/CuO < fBN/ZnO < fBN/ZrO_2-modified composite nanofibers. The increase in Ea can be attributed to the enhancement of intermolecular interaction with PVA and PAA, as well as molecules incorporated into the composite structure with both MOs with fBN/MO modified and fBN/MO particles with green synthesis. The most pronounced impact was observed in nanofibers containing fBN/ZrO_2, while the least significant effect was noted in nanofibers containing CuO. However, positive ΔH and ΔG values indicate that energy is required for decomposition. Negative ΔS values suggest that the products exhibit lower disorder compared to the initial conditions, indicating a reduction in entropy due to bond breaking.

The FTIR spectra of PVA/PAA and fBN/MO-modified composite nanofibers are shown in Figure 5d. The stretching vibration of −OH in the molecular skeletons of PVA and PAA correlates with the wide band at 3372 cm^{-1}; the stretching vibration of C═O corresponds to the band at 1718 cm^{-1}. The stretching vibrations of C−O and C−H align with the bands at 1247 and 2925 cm^{-1}, respectively. The bands in the range of 400−500 cm^{-1} are attributed to the characteristic absorption of the M−O stretching vibrations.[70] The stretching and bending vibrations of BN were observed at approximately 1390 and 850 cm^{-1}, respectively.[61]

The effect of fBN/MO nanoparticles on the TC of PVA/PAA nanofibers was also investigated (Table 1). The TC of the PVA/PAA nanofiber is 0.063 W/mK, whereas fBN/MO-modified PVA/PAA nanofibers have higher TC values. The TC of fBN/ZrO_2-modified composite nanofibers did not change as much as the other MO-modified composite nanofibers due to the different morphology of ZrO_2 moieties. According to the SEM micrographs of fBN/MOs given in Figure 4, fBN/ZrO_2 has a comprehensive and hollow surface resembling the petals of a flower (Figure 4c). In contrast, the other MOs have spherical-like structures. Therefore, fBN/CuO and fBN/ZnO particles do not contribute to the heat

https://doi.org/10.1021/acsapm.3c03226
ACS Appl. Polym. Mater. 2024, 6, 3942−3955

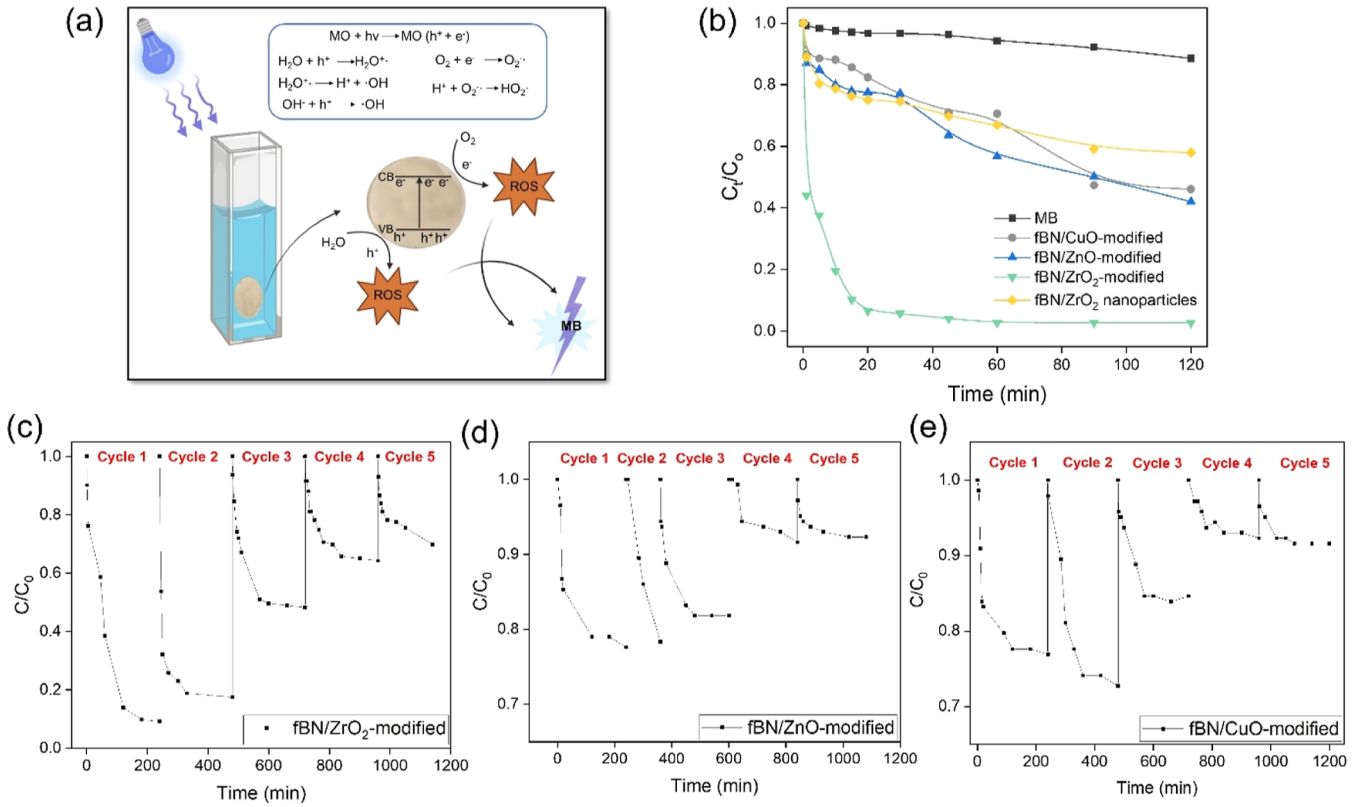

Figure 7. Schematic representation of the photodegradation mechanism (a), normalized concentration with irradiation time (b), and repetitive photodegradation of MB using fBN/ZrO_2- (c), fBN/ZnO- (d), and fBN/CuO- modified nanofibers (e). (Concentration of MB: 50 ppm, pH: 7.0, catalyst dosage: 1.0 g/L, UV−vis irradiation at room temperature.)

conduction pathways as much as fBN/CuO and fBN/ZnO particles. Although the TC decreases in the case of MOs,[71] the increase in TC of fBN/MO-modified nanofibers is mainly caused by the high TC of BN.[72]

Various nanostructures such as Cu, CuO, Al_2O_3, TiO_2, Fe_3O_4, SiC, ZnO, and CNT have been used as thermal conductors, especially in nanofluids.[73] The characteristics, including the quantity and shape of dispersed particles, as well as the type of material, play a crucial role in influencing the TC in materials containing thermal conductors.[74] As an example, Liu et al. demonstrated that in their study, the TC of ethylene glycol, initially at 0.25 W/mK, increased by 4% with the addition of 1% CuO nanoparticles (theoretical TC: 33 W/mK). Moreover, the TC showed a more substantial increase of 22.4% when the amount of CuO nanoparticles was increased to 5%.[75] In another study, the impact of the morphology of ZnO nanoparticles on the TC of water was explored. In two systems containing spherical- and rectangular-shaped ZnO nanoparticles (5%), the TC of water increased by 12 and 18%, respectively.[73] In a different study, it was noted that the density serves as a crucial parameter for ZrO_2 nanoparticles, highlighting that the increment in the relative density of ZrO_2 nanoparticles improves the TC.[76]

Antibacterial/Antioxidant Activity of Nanofibers. The bacterial inhibition activity of fBN/MO-modified nanofibers was investigated against *S. mutans*, *A. baumannii*, *S. aureus*, and *E. coli* (Figure 6a). The composite nanofibers exhibited a wide-ranging efficacy, diminishing the number of viable colonies. The antibacterial activity of all fBN/MO-modified composite nanofibers ranges between 99.7 and 99.9%, showing high antibacterial activity against *S. mutans* and *A. baumannii*. Similar to their effectiveness against *S. mutans* and *A. baumannii*, fBN/MO-modified composite nanofibers exhibited notable activity (98.8−99.9%) against *S. aureus* and *E. coli*. The fBN/CuO-modified nanofibers guarantee the inhibition of bacteria by inducing denaturation of essential enzymes. Additionally, the bacterial inhibition activity of ZnO nanoparticles primarily stems from the formation of reactive oxygen species (ROS), the release of zinc ions, and membrane dysfunction, while ZrO_2 nanoparticles cause the death of microorganisms due to electromagnetic attraction. Overall, antibacterial activity mechanisms of metal/MO nanoparticles can be outlined as the generation of ROS facilitated by nanoparticles, release of ions, cell wall fragmentation resulting from nanoparticle entry into the cell, denaturation of enzymes and proteins, hindrance of DNA replication and induction of DNA damage, and disruption of essential cellular functions through the limitation of electron transfer within the cell (Figure 6b).

In our previous study, PVA/PAA nanofibers showed relatively weak antibacterial activity against both *E. coli* and *S. aureus*, and by incorporating BN nanoparticles, the antibacterial activity was enhanced.[40] A further improvement in antibacterial activity was achieved with implementation of the MOs. The functional groups on the MOs, originating from both BN modification and reduction by the *S. rebaudiana* extract, enhance the ability of nanoparticles to bind to the bacterial cell membrane. Subsequently, the released M^{n+} ions from the nanoparticles engage with sulfhydryl groups and phosphorus-containing compounds in the membrane, disrupting DNA replication and inducing oxidative stress. Besides surface modification, the antibacterial properties of MO

https://doi.org/10.1021/acsapm.3c03226
ACS Appl. Polym. Mater. 2024, 6, 3942−3955

nanoparticles are also influenced by a complex interplay of factors, including their size, surface charge, composition, crystalline structure, concentration, exposure time, bacterial sensitivity, and environmental conditions.[77] Azam et al. investigated the antibacterial activity of CuO nanoparticles against bacteria and emphasized the dependency of particle size, stability, and concentration on the bacterial growth medium.[78] Apart from MO nanoparticles, metal nanoparticles such as Ag, Cu, Au, Pd, and MOs containing a polymer composite have been used to enhance the antibacterial activity.[79]

The antioxidant activity of nanomaterials refers to their ability to neutralize or counteract oxidative stress in biological systems. Nanomaterials with antioxidant properties can scavenge ROS and free radicals, which are highly reactive molecules that can cause cellular damage. The unique properties of nanomaterials, such as their high surface area to volume ratio and tunable surface chemistry, make them promising candidates for antioxidant applications.[80] Figure 6c shows the antioxidant activity of the fBN/MO-modified composite nanofibers. The % RSA values are 0.86 ± 0.156, 26.62 ± 0.21, 9.36 ± 1.04, and 11.23 ± 0.72 for neat, fBN/CuO, fBN/ZnO, and fBN/ZrO_2-modified composite nanofibers (at 10 mg), respectively. The increased antioxidant efficacy of nanofibers can be ascribed to the radical quenching impact of the unpaired electrons in MO nanoparticles, coupled with their substantial surface area.[81] The enhanced antioxidant potential observed in composite nanofibers modified with fBN/CuO (due to its lower calcination temperature) compared to fBN/ZnO and fBN/ZrO_2 can be linked to the presence of secondary metabolites derived from *S. rebaudiana*, as evidenced by the FTIR spectrum of the fBN/CuO nanoparticles (see Figure 3c). Analogously, Nazir et al. noted a comparable scenario, with the antioxidant activity of CuO NPs surpassing that of MnO NPs.[82] In an alternate investigation conducted by Adeyemi et al., CuO NPs demonstrated superior antioxidant activity in comparison to ZnO NPs. Additionally, the antioxidant activity of the NPs exhibited an incremental trend with increasing concentration.[83] Rehman et al. reported that CuO NPs synthesized using the *Bergenia ciliata* extract quenched 30.36% of $ABTS^{+*}$ radical when used at a concentration of 25 μg/mL and 88.7% at a concentration of 400 μg/mL.[84] Moreover, the activity of ZnO nanoparticles synthesized using the *Simarouba glauca* extract (100 μg/mL) against different radical species (DPPH, ABTS, peroxide, and superoxide) showed the highest %RSA value for peroxide.[85] Another study reported that ZnO−ZrO_2 heterooxide produced by the extract of Ficus elastic leaves showed 25.87% radical quenching against $ABTS^{+*}$.[86] The AEAC values are 0.089, 3.796, 1.405, 1.674, and 1.000 for PVA/PAA, fBN/CuO, fBN/ZrO_2, fBN/ZnO-modified composite nanofibers, and L-ascorbic acid, respectively. Accordingly, PVA/PAA exhibited no antioxidant capacity, whereas the antioxidant capacity exhibited an increase in the case of fBN/MO-modified composite nanofibers. This augmentation is attributed to the electron-donating property of the oxygen atom within the MO, enabling the regulation of free radicals that may induce oxidative stress.[87]

Photocatalytic Activity of Nanofibers. The photocatalytic activities of fBN/MO-modified composite nanofibers were determined by MB under UV light. Figure 7a shows that the photodegradation of organic compounds occurs spontaneously (photolysis) or in the presence of a photocatalyst under UV light, forming electrons (e^-) and holes (h^+). Hydroxyl radicals ($^{\bullet}OH$) and H^+ ions are obtained from the H_2O-formed holes. The resulting $^{\bullet}OH$ plays an active role in the degradation of the dye.[88]

The photocatalytic efficiency of fBN/MO-modified nanofibers in MB degradation was assessed by monitoring the time-dependent reduction in absorption maxima at 664 nm, indicative of MB. The degradation process showed a steady decline with increasing time in the presence of fBN/MO-modified nanofibers, reaching equilibrium after 20 min (Figure S5). MB photolysis was negligible, however, in the presence of the catalyst, degradation increases considerably. The most significant decrease among fBN/MO-modified nanofibers was observed for fBN/ZrO_2-modified ones. The percent degradation in the absence of the fiber catalyst was 5.78%, and it was 53.89, 57.96, and 97.56% in the presence of fBN/CuO, fBN/ZnO, and fBN/ZrO_2-modified nanofibers, respectively.

Figure 7b shows the photocatalytic activity of the fBN/MO-modified nanofibers; the degradation of MB was investigated and compared with that of the fBN/ZrO_2 nanoparticles. As expected, the decay of absorbance intensity at time t over initial intensity (C_t/C_0 = 0.89) is slower for the photolysis. This ratio decreases to 0.46, 0.42, and 0.027 for fBN/CuO-, fBN/ZnO-, and fBN/ZrO_2-modified nanofibers, respectively. The maximum degradation occurred in the presence of the fBN/ZrO_2-modified nanofiber catalyst. For this reason, the fBN/ZrO_2 nanoparticle was also used as a catalyst (C_t/C_0 = 0.58), indicating that the catalyst efficiency increased in the nanofiber form. Pantò et al. investigated various ZnO nanostructure morphologies for MB degradation to clarify the photocatalysis properties. ZnO nanofibers were reported to be the most efficient photocatalyst compared to microflowers and commercial nanoparticles. The increased degradation efficiency has been attributed to a larger specific surface area and a higher density of active sites available for dye adsorption.[89] Furthermore, the doping process can also modify the surface area and improve defects and vacancies in the MO lattice. These defects can serve as active sites for catalytic reactions, further enhancing the photocatalytic activity.[90] According to Nasr et al., BN doping increased the oxygen vacancies on the TiO_2 nanofiber surface, which can also be viewed as a recombination of free electrons with trapped holes.[91]

On the one hand, the band gap of a photocatalyst directly influences its ability to absorb light, generate electron−hole pairs, prevent recombination, drive redox reactions, and determine the selectivity of the degradation process.[88] The band gap energy of fBN/MO nanoparticles was calculated using Tauc's formula.[92] The higher photocatalytic efficiency of the fBN/ZrO_2 (2.75 eV) nanoparticles compared to fBN/CuO (4.10 eV) and fBN/ZnO (4.60 eV) can be attributed to the band gap energy values. This also increases the charge separation capability and provides a way to improve the separation efficiency of photogenerated electron−hole pairs.[91] On the other hand, a red shift in the band gap energy increases the visible absorption at the interface of BN and MOs. The photogenerated electrons can be delocalized in the $\pi-\pi$ conjugated system of BN, and the electron−hole pair's recombination rate will be delayed, leading to increased photocatalytic activity.[93] Sayegh et al. emphasized the separation efficiency of BN doping on the photocatalytic performance of TiO_2 nanofibers.[94] The rate constants for the MB degradation are determined to be 0.87 × 10^{-3}, 6.32

https://doi.org/10.1021/acsapm.3c03226
ACS Appl. Polym. Mater. 2024, 6, 3942−3955

Table 2. Degradation Efficiency and Comparison of Studies with Different MO/BN Nanofibers Photocatalysts

pollutant	$C_{Pollutant}$ (mg/L)	photocatalyst	$C_{Photocatalyst}$ (g/L)	polymer/solvent	synthesis method	irradiation type	energy, (W/m^2)	removal efficiency, %	degradation time (min)	pH	ref
methyl orange	10	BN (10 wt %)/TiO_2	0.4	TTIP/PVP (0.3 g)/ethanol (5 mL)/acetic acid (2 mL)	electrospinning and sol−gel	UV light irradiation (462 nm)	N.A	99	75		91
ACT	1	TiO_2−BN−Pd	0.5	TTIP/PVP (0.3 g)/ethanol/acetic acid (2 mL)	atomic layer deposition of BN and Pd electrospinning	UV and visible light	400 W	100 (UV)	10 (UV)	6.8	94
						UV lamp and linear halogen lamp		98 (Vis)	180 (Vis)		
MB	20	BN (5 wt %)−Ag (3 wt %)/TiO_2	0.4	TTIP/PVP (0.3 g)/ethanol (5 mL)/acetic acid (2 mL)	electrospinning and sol−gel	visible light (>400 nm)	150 W	98 (MB)	80		96
E. coli ibuprofen	5	TiO_2-BN	0.2	TTIP/PVP (0.3 g)/ethanol (5 mL)/acetic acid (2 mL)	electrospinning and sol−gel	UV light irradiation (365 nm)	N.A	98	180	7	97
						visible light (405, 435, and 545 nm)					
ibuprofen	5	TiO_2−BN (10 wt %)	0.2	TTIP/PVP (0.3 g)/ethanol (5 mL)/acetic acid (2 mL)	electrospinning and sol−gel	visible light irradiation, halogen lamp	150 W	100	120	7	98
acetaminophen (ACT)	10	BN/TiO_2/HNT	0.5	poly(vinylpyrrolidone) (PVP) (10%)/ethanol	electrospinning and sol−gel	visible light	400 W	99	180	7	99
						Linear, halogen lamp					
dyes (RB, MV, CR) and antibiotics (CIP, TC)	∼6	B−C_3N_4	1.0	polyethersulfone (PES) PVP/DMAc and dichloromethane	electrospinning	visible light	500 W	100	15	6.0	100
						irradiation					
						xenon lamp					
dyes (RB, MB, ST, MV, MG) and antibiotics (CIP, TC)	∼10	B−C_3N_4 (1.9 wt %)	∼3	PES (19 wt %) and p(MMA-AA) copolymer (1.9 wt %)/DMAc	electrospinning	visible light	N.A	100	240	5.3	101
						irradiation					
						xenon lamp					
MB	50	fBN/CuO-, fBN/ZnO-, fBN/ZrO_2-modified	1.0	PVA (20 wt %)/PAA (1 wt %)/DW	electrospinning	UV−vis irradiation (360 nm)	8 W	53.89 (fBN/CuO-)	20	7.0	this study
								57.96 (fBN/ZnO-)			
								97.56% (fBN/ZrO_2-modified)			

https://doi.org/10.1021/acsapm.3c03226
ACS Appl. Polym. Mater. 2024, 6, 3942−3955

$\times 10^{-3}$, 6.51×10^{-3}, 123×10^{-3}, and 11.8×10^{-3} min^{-1} for photolysis, fBN/CuO-, fBN/ZnO-, fBN/ZrO_2-modified nanofibers, and fBN/ZrO_2 nanoparticles, respectively, with the highest R^2 values. The linearity in the kinetic plots was confirmed that the photodegradation of MB fitted the first-order kinetics (Figure S6). Accordingly, the rapid degradation rate belongs to the fBN/ZrO_2-modified nanofiber due to the aforementioned morphological and optoelectronic features.

Figure 7c shows the reusability of the fBN/MO-modified nanofibers by the recycling experiments for 5 cycles. Generally, the MB degradation rate remained almost unchanged for the first two cycles of fBN/MO-modified nanofibers, especially for fBN/ZrO_2-modified nanofibers that are more stable and can be used for repeated treatment of MB at least three times. A decrease in catalytic activity may be related to the experimental conditions such as the type of dye, pH, temperature, light intensity, dosage, and morphology of the catalyst.[95]

Table 2 presents a compilation of studies investigating the photocatalytic properties of various MO/BN nanofibers prepared through electrospinning. Nasr et al. recommended the utilization of BN/TiO_2 nanofibers for the photocatalytic degradation of methyl orange. Their findings indicated that BN/TiO_2 nanofibers exhibited superior activity compared to neat TiO_2.[91] The same group of authors used BN-Ag/TiO_2 nanofibers obtained by incorporating Ag precursor into the system for both MB degradation and the investigation of its antibacterial activity against *E. coli*. They highlighted the improved photocatalytic and antibacterial activity of TiO_2 nanofibers with the addition of BN and Ag nanostructures.[96] In another study, BN/TiO_2 nanofibers were used for photocatalytic oxidation of ibuprofen under UV irradiation.[97] In addition, Lin et al. performed this study under visible light to demonstrate their usability as solar photocatalysts, especially in the treatment of real wastewater.[98] Similarly, under both UV and visible light, Sayegh et al. used TiO_2-BN-Pd nanofibers for the degradation of ACT. Differently, they modified the TiO_2 nanofibers by BN and Pd through atomic layer deposition.[94] Another study reported that BN/TiO_2/HNT composite nanofibers exhibited a high degradation rate for ACT under visible light.[99] Xu et al. suggested using B−C_3N_4-based nanofibers with two different template polymers (polyethersulfone with poly(vinyl pyrrolidone)[100] or poly(methyl methacrylate-*co*-acrylic acid))[101] for adsorption and photocatalysis of different dyes and antibiotics.

The literature primarily revolves around electrospinning metal precursors, additives, and polymers, followed by calcination to achieve the MO composite nanofibers. However, the high temperature applied during the calcination process deteriorates the mechanical integrity of the resulting nanofibers, making them brittle. Therefore, we first synthesized the fBN/MO nanoparticles before electrospinning proceeded by low-temperature thermal cross-linking.

CONCLUSIONS

Phytosynthesized CuO, ZnO, and ZrO_2 nanoparticles were decorated on the fBN nanoparticles, followed by incorporation into the electrospun PVA/PAA composite nanofibers. The morphological investigation showed the randomly distributed fBN/CuO and fBN/ZnO nanoparticles with irregular geometry as well as polygonal-shaped fBN/ZrO_2 nanoparticles. fBN/MO nanoparticles were homogeneously distributed along the composite nanofiber at the designated concentration. The impact of fBN/MO nanoparticles on the thermal properties of the neat nanofiber was examined in terms of the stability and conductivity of fBN/MO-modified composite nanofibers. The incorporation of fBN/MO nanoparticles into the composite nanofibers improved their thermal stability and conductivity compared to the PVA/PAA nanofibers. The enhanced thermal stability was also supported by changes in thermodynamic functions. fBN/MO-modified composite nanofibers demonstrated high antibacterial efficacy against *S. mutans*, *A. baumannii*, *E. coli*, and *S. aureus*, while concurrently enhancing their antioxidant properties. The effective photocatalytic remediation to MB using fBN/MO-modified composite nanofibers was observed. fBN/ZrO_2-modified composite nanofibers exhibited the highest photocatalytic activity because of their morphological and optoelectronic properties. The transformation of the fBN/ZrO_2 nanoparticles into nanofibers resulted in a more than 20-fold improvement in photocatalytic degradation efficiency. Besides, they demonstrated enhanced stability, allowing for repeated treatment of MB for a minimum of three cycles. Multifunctional fBN/MO-modified composite nanofibers exhibit antibacterial, antioxidant, and photodegradation activity, making them suitable for applications in biomaterials and water disinfection.

ASSOCIATED CONTENT

Supporting Information

The Supporting Information is available free of charge at https://pubs.acs.org/doi/10.1021/acsapm.3c03226.

UV−vis spectra of *S. rebaudiana* and/or metal precursors and MO nanoparticles, FTIR spectra of *S. rebaudiana*, fBN/M(OH)n, and fBN/MO nanoparticles, EDS spectra of fBN/MO nanocomposites, EDS mapping and spectra of fBN/MO-modified PVA/PAA nanofibers, and UV−vis spectra of MB solutions in the presence of fBN/MO-modified nanofibers (PDF)

AUTHOR INFORMATION

Corresponding Author

Ayşegül Ülkü Metin − *Department of Chemistry, Faculty of Engineering and Natural Sciences, Kırıkkale University, Yahşihan 71450 Kırıkkale, Turkey;* orcid.org/0000-0001-8494-601X; Email: aumetin@kku.edu.tr

Authors

Nesrin Horzum − *Department of Engineering Sciences, Faculty of Engineering and Architecture, İzmir Katip Çelebi University, 35620 İzmir, Turkey*

Deniz Doğan − *Department of Chemistry, Faculty of Engineering and Natural Sciences, Kırıkkale University, Yahşihan 71450 Kırıkkale, Turkey*

Fatma Rabia Karaduman − *Graduate School of Natural and Applied Sciences, İzmir Katip Çelebi University, 35620 İzmir, Turkey*

Complete contact information is available at: https://pubs.acs.org/10.1021/acsapm.3c03226

Notes

The authors declare no competing financial interest.

ACKNOWLEDGMENTS

The authors gratefully thank Kirikkale University Scientific and Technological Research Application and Research Center and

IZTECH Biotechnology and Bioengineering Application and Research Center for the analysis.

REFERENCES

(1) Madhav, S.; Ahamad, A.; Singh, A. K.; Kushawaha, J.; Chauhan, J. S.; Sharma, S.; Singh, P. Water Pollutants: Sources and Impact on the Environment and Human Health. *Sensors in Water Pollutants Monitoring: Role of Material*, 2020; pp 43−62..

(2) Al-Tohamy, R.; Ali, S. S.; Li, F.; Okasha, K. M.; Mahmoud, Y. A. G.; Elsamahy, T.; Jiao, H.; Fu, Y.; Sun, J. A Critical Review on the Treatment of Dye-Containing Wastewater: Ecotoxicological and Health Concerns of Textile Dyes and Possible Remediation Approaches for Environmental Safety. *Ecotoxicol. Environ. Saf.* **2022**, *231* (113160), 113160.

(3) Moyo, S.; Makhanya, B. P.; Zwane, P. E. Use of Bacterial Isolates in the Treatment of Textile Dye Wastewater: A Review. *Heliyon* **2022**, *8* (6), No. e09632. 1−13

(4) Natarajan, S.; Bajaj, H. C.; Tayade, R. J. Recent Advances Based on the Synergetic Effect of Adsorption for Removal of Dyes from Waste Water Using Photocatalytic Process. *J. Environ. Sci.* **2018**, *65*, 201−222.

(5) Zhou, Y.; Lu, J.; Zhou, Y.; Liu, Y. Recent Advances for Dyes Removal Using Novel Adsorbents: A Review. *Environ. Pollut.* **2019**, *252*, 352−365.

(6) De, A.; Kalita, D.; Jain, P. Biofabricated Silver Nanoparticles and Nanocomposites as Green Catalyst to Mitigate Dye Pollution in Water-A Review. *ChemistrySelect* **2021**, *6* (40), 10776−10787.

(7) Katheresan, V.; Kansedo, J.; Lau, S. Y. Efficiency of Various Recent Wastewater Dye Removal Methods: A Review. *J. Environ. Chem. Eng.* **2018**, *6* (4), 4676−4697.

(8) Hasanpour, M.; Hatami, M. Photocatalytic Performance of Aerogels for Organic Dyes Removal from Wastewaters: Review Study. *J. Mol. Liq.* **2020**, *309*, 113094.

(9) Amakiri, K. T.; Angelis-Dimakis, A.; Ramirez Canon, A. Recent Advances, Influencing Factors, and Future Research Prospects Using Photocatalytic Process for Produced Water Treatment. *Water Sci. Technol.* **2022**, *85* (3), 769−788.

(10) Danish, M. S. S.; Estrella, L. L.; Alemaida, I. M. A.; Lisin, A.; Moiseev, N.; Ahmadi, M.; Nazari, M.; Wali, M.; Zaheb, H.; Senjyu, T. Photocatalytic Applications of Metal Oxides for Sustainable Environmental Remediation. *Metals* **2021**, *11* (1), 80.

(11) Joshi, N. C.; Gururani, P.; Gairola, S. P. Metal Oxide Nanoparticles and Their Nanocomposite-Based Materials as Photocatalysts in the Degradation of Dyes. *Biointerface Res. Appl. Chem.* **2021**, *12* (5), 6557−6579.

(12) Verma, N.; Chundawat, T. S.; Chandra, H.; Vaya, D. An efficient time reductive photocatalytic degradation of carcinogenic dyes by TiO2-GO nanocomposite. *Materials Research Bulletin* **2023**, *158*, 112043.

(13) Jemai, S.; Khezami, L.; Gueddana, K.; Trabelsi, K.; Hajjaji, A.; Amlouk, M.; Soucase, B. M.; Bessais, B.; Rtimi, S. Impact of Annealing on ZrO_2 Nanotubes for Photocatalytic Application. *Catalysts* **2023**, *13* (3), 558.

(14) Chelliah, P.; Wabaidur, S. M.; Sharma, H. P.; Majdi, H. S.; Smait, D. A.; Najm, M. A.; Iqbal, A.; Lai, W. C. Photocatalytic Organic Contaminant Degradation of Green Synthesized ZrO_2 NPs and Their Antibacterial Activities. *Separations* **2023**, *10* (3), 156.

(15) Bibi, I.; Kamal, S.; Abbas, Z.; Atta, S.; Majid, F.; Jilani, K.; Hussain, A. I.; Kamal, A.; Nouren, S.; Abbas, A. A New Approach of Photocatalytic Degradation of Remazol Brilliant Blue by Environment Friendly Fabricated Zinc Oxide Nanoparticle. *Int. J. Sci. Environ. Technol.* **2020**, *17* (3), 1765−1772.

(16) Haspulat Taymaz, B.; Demir, M.; Kamış, H.; Orhan, H.; Aydoğan, Z.; Akıllı, A. Facile and Green Synthesis of ZnO Nanoparticles for Effective Photocatalytic Degradation of Organic Dyes and Real Textile Wastewater. *Int. J. Phytorem.* **2023**, *25* (10), 1306−1317.

(17) Aroob, S.; Carabineiro, S. A. C.; Taj, M. B.; Bibi, I.; Raheel, A.; Javed, T.; Yahya, R.; Alelwani, W.; Verpoort, F.; Kamwilaisak, K.; Al-Farraj, S.; Sillanpää, M. Green Synthesis and Photocatalytic Dye Degradation Activity of CuO Nanoparticles. *Catalysts* **2023**, *13* (3), 502.

(18) Sharma, S.; Kumar, K.; Thakur, N.; Chauhan, S.; Chauhan, M. S. Eco-Friendly Ocimum Tenuiflorum Green Route Synthesis of CuO Nanoparticles: Characterizations on Photocatalytic and Antibacterial Activities. *J. Environ. Chem. Eng.* **2021**, *9* (4), 105395.

(19) Ikram, A.; Jamil, S.; Fasehullah, M. Green Synthesis of Copper Oxide Nanoparticles from Papaya/Lemon Tea Extract and Its Application in Degradation of Methyl Orange. *Mater. Res. Innovat.* **2022**, *02* (04), 115−122.

(20) Borgo, J.; Laurella, L. C.; Martini, F.; Catalán, C. A. N.; Sülsen, V. P. Stevia Genus: Phytochemistry and Biological Activities Update. *Molecules* **2021**, *26* (9), 2733.

(21) Parida, V. K.; Srivastava, S. K.; Gupta, A. K.; Rawat, A. A Review on Nanomaterial-Based Heterogeneous Photocatalysts for Removal of Contaminants from Water. *Mater. Express* **2023**, *13* (1), 1−38.

(22) Jain, M.; Mudhoo, A.; Ramasamy, D. L.; Najafi, M.; Usman, M.; Zhu, R.; Kumar, G.; Shobana, S.; Garg, V. K.; Sillanpää, M. Adsorption, Degradation, and Mineralization of Emerging Pollutants (Pharmaceuticals and Agrochemicals) by Nanostructures: A Comprehensive Review. *Environ. Sci. Pollut. Res.* **2020**, *27*, 34862−34905.

(23) Feng, T.; Cui, J.; Ou, M.; Li, R.; Zhao, Z.; Geng, Y.; Chen, X.; Jiao, C. 0D-2D Nanohybrids Based on Binary Transitional Metal Oxide Decorated Boron Nitride Enabled Epoxy Resin Efficient Flame Retardant Coupled with Enhanced Thermal Conductivity at Ultra-Low Additions. *Compos. Commun.* **2023**, *41*, 101649.

(24) Shirodkar, S. N.; Waghmare, U. V.; Fisher, T. S.; Grau-Crespo, R. Engineering the Electronic Bandgaps and Band Edge Positions in Carbon-Substituted 2D Boron Nitride: A First-Principles Investigation. *Phys. Chem. Chem. Phys.* **2015**, *17* (20), 13547−13552.

(25) Nasr, M.; Viter, R.; Eid, C.; Habchi, R.; Miele, P.; Bechelany, M. Enhanced Photocatalytic Performance of Novel Electrospun BN/TiO_2 Composite Nanofibers. *New J. Chem.* **2017**, *41* (1), 81−89.

(26) Singh, B.; Singh, K.; Kumar, M.; Thakur, S.; Kumar, A. Insights of Preferred Growth, Elemental and Morphological Properties of BN/SnO_2 Composite for Photocatalytic Applications towards Organic Pollutants. *Chem. Phys.* **2020**, *531*, 110659.

(27) Xu, H.; Liu, L.; Song, Y.; Huang, L.; Li, Y.; Chen, Z.; Zhang, Q.; Li, H. BN Nanosheets Modified WO_3 Photocatalysts for Enhancing Photocatalytic Properties under Visible Light Irradiation. *J. Alloys Compd.* **2016**, *660*, 48−54.

(28) Liu, D.; Song, J.; Chung, J. S.; Hur, S. H.; Choi, W. M. ZnO/Boron Nitride Quantum Dots Nanocomposites for the Enhanced Photocatalytic Degradation of Methylene Blue and Methyl Orange. *Molecules* **2022**, *27* (20), 6833.

(29) Horzum, N.; Muñoz-Espí, R.; Glasser, G.; Demir, M. M.; Landfester, K.; Crespy, D. Hierarchically Structured Metal Oxide/Silica Nanofibers by Colloid Electrospinning. *ACS Appl. Mater. Interfaces* **2012**, *4* (11), 6338−6345.

(30) Bhardwaj, N.; Kundu, S. C. Electrospinning: A Fascinating Fiber Fabrication Technique. *Biotechnol. Adv.* **2010**, *28* (3), 325−347.

(31) Asgari, S.; Mohammadi Ziarani, G.; Badiei, A.; Ajalloueian, F.; Vasseghian, Y. Electrospun Composite Nanofibers as Novel High-Performance and Visible-Light Photocatalysts for Removal of Environmental Pollutants: A Review. *Environ. Res.* **2022**, *215*, 114296.

(32) Abid, M.; Sayegh, S.; Tanos, F.; Belaid, H.; Iatsunskyi, I.; Coy, E.; Cretin, M.; Lesage, G.; Ben Haj Amara, A.; Bechelany, M. A Novel BN/TiO_2/HNT Nanocomposite for Photocatalytic Applications Fabricated by Electrospinning. *Colloids Surf. A Physicochem. Eng. Asp.* **2023**, *662*, 131043.

(33) Ghorbanloo, M.; Nada, A. A.; El-Maghrabi, H. H.; Bekheet, M. F.; Riedel, W.; Viter, R.; Roualdes, S.; Miele, P.; Bechelany, M. BN/Cs_2CO_3/TiO_2 Composite Nanofibers to Improve Hydrogen Generation. *J. Alloys Compd.* **2023**, *945*, 169218.

(34) Lin, L.; Jiang, W.; Nasr, M.; Bechelany, M.; Miele, P.; Wang, H.; Xu, P. Enhanced Visible Light Photocatalysis by TiO_2-BN Enabled Electrospinning of Nanofibers for Pharmaceutical Degrada-

https://doi.org/10.1021/acsapm.3c03226
ACS Appl. Polym. Mater. 2024, 6, 3942−3955

tion and Wastewater Treatment. *Photochem. Photobiol. Sci.* **2019**, *18*, 2921−2930.
(35) Sayegh, S.; Tanos, F.; Nada, A.; Lesage, G.; Zaviska, F.; Petit, E.; Rouessac, V.; Iatsunskyi, I.; Coy, E.; Viter, R.; Damberga, D.; Weber, M.; Razzouk, A.; Stephan, J.; Bechelany, M. Tunable TiO_2-BN-Pd Nanofibers by Combining Electrospinning and Atomic Layer Deposition to Enhance Photodegradation of Acetaminophen. *Dalton Trans.* **2022**, *51* (7), 2674−2695.
(36) Xu, Y.; Yuan, D.; Guo, Y.; Chen, S.; Lin, W.; Long, Y.; Bao, J.; He, C.; Cheng, C.; Deng, C.; Zhang, Y.; Wu, Y.; Zhao, W.; Zhao, C. Superhydrophilic and Polyporous Nanofibrous Membrane with Excellent Photocatalytic Activity and Recyclability for Wastewater Remediation under Visible Light Irradiation. *J. Chem. Eng.* **2022**, *427*, 131685.
(37) Ma, Z.; Liu, Z.; Cheng, Z. Scalable Exfoliation for Few-Layered Hexagonal Boron Nitride Nanosheets (BNNSs) by Microwave-Assisted Expansion and Liquid Nitrogen Intercalation. *Chin. Chem. Lett.* **2020**, *31* (7), 1936−1940.
(38) Bayramoglu, G.; Senel, A. U.; Arica, M. Y. Effect of Spacer-Arm and Cu(II) Ions on Performance of l-Histidine Immobilized on Poly(GMA/MMA) Beads as an Affinity Ligand for Separation and Purification of IgG. *Sep. Purif. Technol.* **2006**, *50* (2), 229−239.
(39) Hissay Bhutia, P.; Baran Sharangi, A. IJCST Stevia: Medicinal Miracles and Therapeutic Magic. *Int. J. Crop Sci. Technol.* **2016**, *2* (2), 45−59.
(40) Doğan, D.; Karaduman, F. R.; Horzum, N.; Metin, A. U.·. Boron Nitride Decorated Poly(Vinyl Alcohol)/Poly(Acrylic Acid) Composite Nanofibers: A Promising Material for Biomedical Applications. *J. Mech. Behav. Biomed. Mater.* **2023**, *141*, 105773.
(41) Coats, A. W.; Redfern, J. P. Kinetic Parameters from Thermogravimetric Data. *Nature* **1964**, *201*, 68−69.
(42) Al-Shemy, M. T.; Al-Sayed, A.; Dacrory, S. Fabrication of Sodium Alginate/Graphene Oxide/Nanocrystalline Cellulose Scaffold for Methylene Blue Adsorption: Kinetics and Thermodynamics Study. *Sep. Purif. Technol.* **2022**, *290*, 120825.
(43) Serpen, A.; Gökmen, V.; Pellegrini, N.; Fogliano, V. Direct Measurement of the Total Antioxidant Capacity of Cereal Products. *J. Cereal. Sci.* **2008**, *48* (3), 816−820.
(44) Lagergren, S. About the Theory of So-Called Adsorption of Soluble Substances. *Sven. Vetenskapsakad. Handingarl* **1898**, *24*, 1−39.
(45) Gutiérrez, R.; Martín del Valle, E. M.; Galán, M. A. Immobilized Metal-Ion Affinity Chromatography: Status and Trends. *Sep. Purif. Rev.* **2007**, *36* (1), 71−111.
(46) Gupta, A.; Jain, R.; Gupta, D. C. Studies on Uptake Behavior of Hg(II) and Pb(II) by Amine Modified Glycidyl Methacrylate-Styrene-N,N′-Methylenebisacrylamide Terpolymer. *React. Funct. Polym.* **2015**, *93* (1), 22−29.
(47) Pearson, R. G. Hard and Soft Acids and Bases, HSAB, Part 1: Fundamental Principles. *J. Chem. Educ.* **1968**, *45* (9), 581.
(48) Metin, A. U.·.; Alver, E. Fibrous Polymer-Grafted Chitosan/Clay Composite Beads as a Carrier for Immobilization of Papain and Its Usability for Mercury Elimination. *Bioprocess Biosyst. Eng.* **2016**, *39* (7), 1137−1149.
(49) Yilmaz, M.; Turkdemir, H.; Kilic, M. A.; Bayram, E.; Cicek, A.; Mete, A.; Ulug, B. Biosynthesis of Silver Nanoparticles Using Leaves of *Stevia Rebaudiana*. *Mater. Chem. Phys.* **2011**, *130* (3), 1195−1202.
(50) Sivaraj, R.; Rahman, P. K. S. M.; Rajiv, P.; Narendhran, S.; Venckatesh, R. Biosynthesis and Characterization of Acalypha Indica Mediated Copper Oxide Nanoparticles and Evaluation of Its Antimicrobial and Anticancer Activity. *Spectrochim. Acta, Part A* **2014**, *129*, 255−258.
(51) Anandan, K.; Rajesh, K.; Rajendran, V. Enhanced Optical Properties of Spherical Zirconia (ZrO_2) Nanoparticles Synthesized via the Facile Various Solvents Mediated Solvothermal Process. *J. Mater. Sci. Mater. Electron.* **2017**, *28* (22), 17321−17330.
(52) Pudukudy, M.; Yaakob, Z. Facile Synthesis of Quasi Spherical ZnO Nanoparticles with Excellent Photocatalytic Activity. *J. Cluster Sci.* **2015**, *26* (4), 1187−1201.
(53) Nadeem, A.; Raza, M. A.; Maqsood, M. F.; Ilyas, M. T.; Westwood, A.; Rehman, Z. U. Characterization of Boron Nitride Nanosheets Synthesized by Boron-Ammonia Reaction. *Ceram. Int.* **2020**, *46* (12), 20415−20422.
(54) Alansy, A. S.; Saeed, T. A.; Al-Attab, R.; Guo, Y.; Yang, Y.; Liu, B.; Fan, Z. Boron Nitride Nanosheets Modified with Zinc Oxide Nanoparticles as Novel Fillers of Dental Resin Composite. *Dent. Mater.* **2022**, *38* (10), e266−e274.
(55) Sk, S.; Tiwari, A.; Abraham, B. M.; Manwar, N.; Perupogu, V.; Pal, U. Constructing Cu/BN@PANI Ternary Heterostructure for Efficient Photocatalytic Hydrogen Generation: A Combined Experimental and DFT Studies. *Int. J. Hydrogen Energy* **2021**, *46* (54), 27394−27408.
(56) Bin Mobarak, M.; Hossain, M. S.; Chowdhury, F.; Ahmed, S. Synthesis and Characterization of CuO Nanoparticles Utilizing Waste Fish Scale and Exploitation of XRD Peak Profile Analysis for Approximating the Structural Parameters. *Arab. J. Chem.* **2022**, *15* (10), 104117.
(57) Jiménez-Rosado, M.; Gomez-Zavaglia, A.; Guerrero, A.; Romero, A. Green Synthesis of ZnO Nanoparticles Using Polyphenol Extracts from Pepper Waste (*Capsicum Annuum*). *J. Clean. Prod.* **2022**, *350*, 131541.
(58) Kim, M. G.; Kang, J. M.; Lee, J. E.; Kim, K. S.; Kim, K. H.; Cho, M.; Lee, S. G. Effects of Calcination Temperature on the Phase Composition, Photocatalytic Degradation, and Virucidal Activities of TiO_2 Nanoparticles. *ACS Omega* **2021**, *6* (16), 10668−10678.
(59) Horti, N. C.; Kamatagi, M. D.; Nataraj, S. K.; Wari, M. N.; Inamdar, S. R. Structural and Optical Properties of Zirconium Oxide (ZrO_2) Nanoparticles: Effect of Calcination Temperature. *Nano Express* **2020**, *1* (1), 010022.
(60) Silva Junior, E.; Antonio, S. G.; Longo, E. Synthesis and Structural Evolution of Partially and Fully Stabilized ZrO_2 from a Versatile Method Aided by Microwave Power. *Ceram. Int.* **2018**, *44* (3), 3517−3522.
(61) Sun, G.; Bi, J. Scalable Production of Boron Nitride Nanosheets in Ionic Liquids by Shear-Assisted Thermal Treatment. *Ceram. Int.* **2021**, *47* (6), 7776−7782.
(62) Shaik, M. R.; Alam, M.; Adil, S. F.; Kuniyil, M.; Al-Warthan, A.; Siddiqui, M. R. H.; Tahir, M. N.; Labis, J. P.; Khan, M. Solvothermal Preparation and Electrochemical Characterization of Cubic ZrO_2 Nanoparticles/Highly Reduced Graphene (HRG) Based Nanocomposites. *Materials* **2019**, *12* (5), 711.
(63) Gao, X.; Wang, Y.; Wang, Y.; Wang, Y.; Li, P.; Zhang, Z.; Li, F.; Feng, H.; Li, Z.; Zhang, X. Effect of Copper Oxide@boron Nitride Nanosheet Hybrid Nanocomposite on Tribological Properties of Paraffin Liquid. *SN Appl. Sci.* **2022**, *4*, 212.
(64) Saleh, S. S.; El-Shayeb, N. S. A. Impact of *Spirulina Platensis* and *Stevia Rebaudiana* on Growth and Essential Oil Production of Basil Ocimum Citriodorum. *J. Agric. Rural. Res.* **2020**, *3* (2), 36−45.
(65) Asghar, M. A.; Zahir, E.; Shahid, S. M.; Khan, M. N.; Asghar, M. A.; Iqbal, J.; Walker, G. Iron, Copper and Silver Nanoparticles: Green Synthesis Using Green and Black Tea Leaves Extracts and Evaluation of Antibacterial, Antifungal and Aflatoxin B1 Adsorption Activity. *LWT* **2018**, *90*, 98−107.
(66) Chowdhury, R.; Khan, A.; Rashid, M. H. Green Synthesis of CuO Nanoparticles Using: Lantana Camara Flower Extract and Their Potential Catalytic Activity towards the Aza-Michael Reaction. *RSC Adv.* **2020**, *10* (24), 14374−14385.
(67) Duan, Z. Q.; Liu, Y. T.; Xie, X. M.; Ye, X. Y. A Simple and Green Route to Transparent Boron Nitride/PVA Nanocomposites with Significantly Improved Mechanical and Thermal Properties. *Chin. Chem. Lett.* **2013**, *24* (1), 17−19.
(68) Elkady, M. F.; Hassan, H. S. Photocatalytic Degradation of Malachite Green Dye from Aqueous Solution Using Environmentally Compatible Ag/ZnO Polymeric Nanofibers. *Polymers* **2021**, *13* (13), 2033.
(69) Soytaş, S. H.; Oğuz, O.; Menceloğlu, Y. Z. Polymer Nanocomposites With Decorated Metal Oxides. *Polymer Composites*

https://doi.org/10.1021/acsapm.3c03226
ACS Appl. Polym. Mater. 2024, 6, 3942−3955

with Functionalized Nanoparticles: Synthesis, Properties, and Applications, 2019; pp 287−323..
(70) Otaibi, A. A.; Patil, M. B.; Rajamani, S. B.; Mathad, S. N.; Patil, A. Y.; Amshumali, M. K.; Shaik, J. P.; Asiri, A. M.; Khan, A. Development and Testing of Zinc Oxide Embedded Sulfonated Poly (Vinyl Alcohol) Nanocomposite Membranes for Fuel Cells. *Crystals* **2022**, *12* (12), 1739.
(71) Alade, I. O.; Oyehan, T. A.; Popoola, I. K.; Olatunji, S. O.; Bagudu, A. Modeling Thermal Conductivity Enhancement of Metal and Metallic Oxide Nanofluids Using Support Vector Regression. *Adv. Powder Technol.* **2018**, *29* (1), 157−167.
(72) Feng, M.; Pan, Y.; Zhang, M.; Gao, Q.; Liu, C.; Shen, C.; Liu, X. Largely Improved Thermal Conductivity of HDPE Composites by Building a 3D Hybrid Fillers Network. *Compos. Sci. Technol.* **2021**, *206*, 108666.
(73) Jeong, J.; Li, C.; Kwon, Y.; Lee, J.; Kim, S. H.; Yun, R. Particle Shape Effect on the Viscosity and Thermal Conductivity of ZnO Nanofluids. *Int. J. Refrig.* **2013**, *36* (8), 2233−2241.
(74) Kwak, K.; Kim, C. Viscosity and Thermal Conductivity of Copper Oxide Nanofluid Dispersed in Ethylene Glycol. *Korea Aust. Rheol. J.* **2005**, *17* (2), 35−40.
(75) Liu, M. S.; Lin, M. C. C.; Huang, I. T.; Wang, C. C. Enhancement of Thermal Conductivity with CuO for Nanofluids. *Chem. Eng. Technol.* **2006**, *29* (1), 72−77.
(76) Deng, Z. Y.; Ferreira, J. M. F.; Tanaka, Y.; Isoda, Y. Microstructure and Thermal Conductivity of Porous ZrO_2 Ceramics. *Acta Mater.* **2007**, *55* (11), 3663−3669.
(77) Gautam, S.; Das, D. K.; Kaur, J.; Kumar, A.; Ubaidullah, M.; Hasan, M.; Yadav, K. K.; Gupta, R. K. Transition Metal-Based Nanoparticles as Potential Antimicrobial Agents: Recent Advancements, Mechanistic, Challenges, and Future Prospects. *Discover Nano* **2023**, *18*, 84.
(78) Azam, A.; Ahmed, A. S.; Oves, M.; Khan, M. S.; Memic, A. Size-Dependent Antimicrobial Properties of CuO Nanoparticles against Gram-Positive and -Negative Bacterial Strains. *Int. J. Nanomed.* **2012**, *7*, 3527−3535.
(79) Radulescu, D.-M.; Surdu, V.-A.; Ficai, A.; Ficai, D.; Grumezescu, A.-M.; Andronescu, E. Green Synthesis of Metal and Metal Oxide Nanoparticles: A Review of the Principles and Biomedical Applications. *Int. J. Mol. Sci.* **2023**, *24* (20), 15397.
(80) Valgimigli, L.; Baschieri, A.; Amorati, R. Antioxidant Activity of Nanomaterials. *J. Mater. Chem. B* **2018**, *6*, 2036−2051.
(81) Lizundia, E.; Armentano, I.; Luzi, F.; Bertoglio, F.; Restivo, E.; Visai, L.; Torre, L.; Puglia, D. Synergic Effect of Nanolignin and Metal Oxide Nanoparticles into Poly(l-Lactide) Bionanocomposites: Material Properties, Antioxidant Activity, and Antibacterial Performance. *ACS Appl. Bio Mater.* **2020**, *3* (8), 5263−5274.
(82) Nazir, S.; Jan, H.; Zaman, G.; Khan, T.; Ashraf, H.; Meer, B.; Zia, M.; Drouet, S.; Hano, C.; Abbasi, B. H. Copper Oxide (CuO) and Manganese Oxide (MnO) Nanoparticles Induced Biomass Accumulation, Antioxidants Biosynthesis and Abiotic Elicitation of Bioactive Compounds in Callus Cultures of Ocimum Basilicum (Thai Basil). *Artif. Cells, Nanomed. Biotechnol.* **2021**, *49* (1), 625−633.
(83) Adeyemi, J. O.; Onwudiwe, D. C.; Oyedeji, A. O. Biogenic Synthesis of CuO, ZnO, and CuO-ZnO Nanoparticles Using Leaf Extracts of Dovyalis Caffra and Their Biological Properties. *Molecules* **2022**, *27* (10), 3206.
(84) Rehman, F. U.; Mahmood, R.; Haq, S.; Ahmad, P.; Din, S. U.; Khandaker, M. U.; Idris, A. M.; Zekker, I. Phytogenic Fabrication of Copper Oxide Nanoparticles for Antibacterial and Antioxidant Screening: Physico-Chemical Study. *Crystals* **2022**, *12* (12), 1796.
(85) Hemanth Kumar, N. K.; Murali, M.; Satish, A.; Brijesh Singh, S.; Gowtham, H. G.; Mahesh, H. M.; Lakshmeesha, T. R.; Amruthesh, K. N.; Jagannath, S. Bioactive and Biocompatible Nature of Green Synthesized Zinc Oxide Nanoparticles from Simarouba Glauca DC.: An Endemic Plant to Western Ghats, India. *J. Cluster Sci.* **2020**, *31* (2), 523−534.
(86) Haq, S.; Afsar, H.; Ali, M. B.; Almalki, M.; Albogami, B.; Hedfi, A. Green Synthesis and Characterization of a ZnO-ZrO_2 Heterojunction for Environmental and Biological Applications. *Crystals* **2021**, *11* (12), 1502.
(87) Soren, S.; Kumar, S.; Mishra, S.; Jena, P. K.; Verma, S. K.; Parhi, P. Evaluation of Antibacterial and Antioxidant Potential of the Zinc Oxide Nanoparticles Synthesized by Aqueous and Polyol Method. *Microb. Pathog.* **2018**, *119*, 145−151.
(88) Hilal Elhousseini, M.; Isık, T.; Kap, O.·.; Verpoort, F.; Horzum, N. Dual Remediation of Waste Waters from Methylene Blue and Chromium (VI) Using Thermally Induced ZnO Nanofibers. *Appl. Surf. Sci.* **2020**, *514* (145939), 145939.
(89) Pantò, F.; Dahrouch, Z.; Saha, A.; Patanè, S.; Santangelo, S.; Triolo, C. Photocatalytic Degradation of Methylene Blue Dye by Porous Zinc Oxide Nanofibers Prepared via Electrospinning: When Defects Become Merits. *Appl. Surf. Sci.* **2021**, *557*, 149830.
(90) Qumar, U.; Hassan, J. Z.; Bhatti, R. A.; Raza, A.; Nazir, G.; Nabgan, W.; Ikram, M. Photocatalysis vs Adsorption by Metal Oxide Nanoparticles. *J. Mater. Sci. Technol.* **2022**, *131*, 122−166.
(91) Nasr, M.; Viter, R.; Eid, C.; Habchi, R.; Miele, P.; Bechelany, M. Enhanced Photocatalytic Performance of Novel Electrospun BN/TiO_2 Composite Nanofibers. *New J. Chem.* **2017**, *41* (1), 81−89.
(92) Tauc, J.; Menth, A.; Wood, D. L. Optical and Magnetic Investigations of The Localized States in Semiconducting Glasses. *Phys. Rev. Lett.* **1970**, *25* (11), 749−752.
(93) Singh, B.; Kaur, G.; Singh, P.; Singh, K.; Sharma, J.; Kumar, M.; Bala, R.; Meena, R.; Sharma, S. K.; Kumar, A. Nanostructured BN-TiO_2 Composite with Ultra-High Photocatalytic Activity. *New J. Chem.* **2017**, *41* (20), 11640−11646.
(94) Sayegh, S.; Tanos, F.; Nada, A.; Lesage, G.; Zaviska, F.; Petit, E.; Rouessac, V.; Iatsunskyi, I.; Coy, E.; Viter, R.; Damberga, D.; Weber, M.; Razzouk, A.; Stephan, J.; Bechelany, M. Tunable TiO_2-BN-Pd Nanofibers by Combining Electrospinning and Atomic Layer Deposition to Enhance Photodegradation of Acetaminophen. *Dalton Trans.* **2022**, *51*, 2674−2695.
(95) Gusain, R.; Kumar, N.; Ray, S. S. Factors Influencing the Photocatalytic Activity of Photocatalysts in Wastewater Treatment. *Photocatalysts in Advanced Oxidation Processes for Wastewater Treatment*, 2020; pp 229−270..
(96) Nasr, M.; Soussan, L.; Viter, R.; Eid, C.; Habchi, R.; Miele, P.; Bechelany, M. High Photodegradation and Antibacterial Activity of BN-Ag/TiO_2 Composite Nanofibers under Visible Light. *New J. Chem.* **2018**, *42*, 1250−1259.
(97) Lin, L.; Jiang, W.; Bechelany, M.; Nasr, M.; Jarvis, J.; Schaub, T.; Sapkota, R. R.; Miele, P.; Wang, H.; Xu, P. Adsorption and Photocatalytic Oxidation of Ibuprofen Using Nanocomposites of TiO_2 Nanofibers Combined with BN Nanosheets: Degradation Products and Mechanisms. *Chemosphere* **2019**, *220*, 921−929.
(98) Lin, L.; Jiang, W.; Nasr, M.; Bechelany, M.; Miele, P.; Wang, H.; Xu, P. Enhanced Visible Light Photocatalysis by TiO_2-BN Enabled Electrospinning of Nanofibers for Pharmaceutical Degradation and Wastewater Treatment. *Photochem. Photobiol. Sci.* **2019**, *18*, 2921−2930.
(99) Abid, M.; Sayegh, S.; Tanos, F.; Belaid, H.; Iatsunskyi, I.; Coy, E.; Cretin, M.; Lesage, G.; Ben Haj Amara, A.; Bechelany, M. A Novel BN/TiO_2/HNT Nanocomposite for Photocatalytic Applications Fabricated by Electrospinning. *Colloids Surf. A Physicochem. Eng. Asp.* **2023**, *662*, 131043.
(100) Xu, Y.; Yuan, D.; Guo, Y.; Chen, S.; Lin, W.; Long, Y.; Bao, J.; He, C.; Cheng, C.; Deng, C.; Zhang, Y.; Wu, Y.; Zhao, W.; Zhao, C. Superhydrophilic and Polyporous Nanofibrous Membrane with Excellent Photocatalytic Activity and Recyclability for Wastewater Remediation under Visible Light Irradiation. *J. Chem. Eng.* **2022**, *427*, 131685.
(101) Xu, Y.; Lin, W.; Yuan, D.; Chen, S.; Li, F.; Long, Y.; He, C.; Zhao, W.; Zhao, C. "1 + 1 > 2": Highly Efficient Removal of Organic Pollutants by Composite Nanofibrous Membrane Based on the Synergistic Effect of Adsorption and Photocatalysis. *J. Mater. Sci. Technol.* **2022**, *124*, 76−85.

https://doi.org/10.1021/acsapm.3c03226
ACS Appl. Polym. Mater. 2024, 6, 3942−3955